

# **Development of a Nanoplasmonic Ruler**

## **Biosensing at the Subnanoscale**

Master's thesis in Nanotechnology

Padraic O'Reilly

# THESIS FOR THE DEGREE OF MASTER OF SCIENCE OF NANOTECHNOLOGY

Development of a Nanoplasmonic Ruler – Biosensing at the Subnanoscale  
Padraic O'Reilly  
Göteborg 2017

© Padraic O'Reilly, 2017

Supervisor: Ferry Nugroho, Chemical Physics  
Examiner: Christoph Langhammer, Chemical Physics

Department of Physics  
Chalmers University of Technology  
SE-41296 Göteborg  
Telephone +46 (0)31 772 1000

Cover photo: Top left: The shape of a typical extinction spectrum for a dual-sized nanoantenna ruler  
Top right: An SEM image of dual-sized nanodisks prior to embedding in a dielectric layer  
Bottom middle: An illustration of dual-sized disks embedded in a dielectric layer upon which lipids are adsorbing  
Printed by: Reproservice, Chalmers University of Technology

## **Abstract**

The ability to simultaneously and independently measure the refractive index and thickness of a thin film is of tremendous interest in the fields of material science and biology. For example, via these measurements it can be possible to thoroughly investigate the effects of temperature on a material or the conformational changes of a cell membrane upon the binding of a protein. In this thesis, a dual parametric nanoplasmonic ruler has been developed to enable this simultaneous and independent measurement. A ruler based on a dual-sized nanodisks design has been explored and successfully fabricated using hole-mask colloidal lithography. Milling parameters have been optimised to enable the formation of a topographically flat surface on these rulers. The fabricated rulers have been characterised using atomic force microscopy, scanning electron microscopy, spectrophotometry and bulk refractive index sensitivity measurements. The functionality of the ruler has been tested using lipid adsorption followed by the subsequent binding of DNA and proteins.

## Acknowledgements

First and foremost, I would like to thank Christoph Langhammer for the opportunity to work with his group on this exciting and challenging project. The work environment that you have cultivated for your group is a pleasure to be a part of and is a credit to you.

I feel like I cannot thank my supervisor, Ferry Nugroho, enough. Your patience throughout this project has been unending, which was perhaps necessary when supervising me! You were constantly available to help, regardless of the magnitude of the problem, and I am extremely grateful for this. It was also great to be able to talk football with a fellow United fan, there are not as many of us around as there used to be!

I would like to thank Antonius Armanious for the many biological samples that you provided us with, but also for your patience and your expertise. Your office door was always open to me and for this I am indebted.

Thank you to the Chalmers cleanroom staff for all the great work that they do, especially Mats and Piotr for all the extra help that you afforded me.

Also, a big thank you to everyone in the Langhammer group and Chemical Physics division for your help with all the hurdles I encountered along the way. Especially to Joachim Fritzsche for your expert advice in the various nanofabrication processes that we used over the course of the project.

I would also like to thank my family and friends for your support over the last two years, especially my parents, who have supported me for a lot longer than that in everything I decide to do. And finally, Alisa, you have had to put up with me more than anyone over these two years and I will never know how you did that! Thank you for always being there.

## TABLE OF CONTENTS

<b>1. INTRODUCTION.....</b>	<b>1</b>
LOCALIZED SURFACE PLASMON RESONANCE.....	1
NANOPLASMONIC SENSING .....	2
PROJECT AIM .....	4
<b>2. THEORY .....</b>	<b>5</b>
PLASMONS AND THEIR INTERACTION WITH LIGHT .....	5
LOCALIZED SURFACE PLASMA RESONANCE .....	8
LSPR FOR BIOSENSING .....	9
DUAL-SIZED NANOANTENNAS .....	11
<b>3. FABRICATION .....</b>	<b>14</b>
HOLE-MASK COLLOIDAL LITHOGRAPHY [28] .....	14
PLASMA ENHANCED CHEMICAL VAPOUR DEPOSITION .....	19
ION BEAM MILLING .....	21
<b>4. CHARACTERISATION .....</b>	<b>23</b>
SPECTROPHOTOMETRY .....	23
ATOMIC FORCE MICROSCOPY .....	24
SCANNING ELECTRON MICROSCOPY .....	26
BULK REFRACTIVE INDEX SENSITIVITY .....	28
<b>5. ADSORPTION MEASUREMENT .....</b>	<b>30</b>
EQUIPMENT .....	30
ADSORPTION MEASUREMENT METHODOLOGY .....	31
<b>6. RESULTS AND DISCUSSION .....</b>	<b>37</b>
FABRICATION.....	37
MILLING.....	41
ADSORPTION MEASUREMENTS .....	45
<b>7. CONCLUSION.....</b>	<b>52</b>
OUTLOOK.....	52
<b>8. BIBLIOGRAPHY .....</b>	<b>54</b>

# 1. Introduction

For millennia, the ability to accurately measure a multitude of parameters has been imperative to the advancement of mankind. Some of the most enduring monuments of previous civilisations would not have been possible without even the simplest of measurement techniques and units. Often this was accomplished using what was most readily at hand and in many cases this was literal. The ancient Egyptians and Romans both used units of length such as palms and fingers and were responsible for the construction of vast structures like the Great Pyramids and the Colosseum. As engineering projects became more advanced, from bridges and railways to combustion and jet engines, the demand for increasingly accurate instruments for measuring length and thickness grew. This demand was met with instruments such as calipers, laser rangefinders and interferometers. Developments such as these could actually be viewed as a virtuous circle, where advances in engineering improves measurement techniques which in turn drives further advancements. One example of this is nanotechnology.

Nanotechnology is science and engineering at a scale where at least one dimension of a sample is in the range of 1-100 nanometers. One nanometer is approximately 100,000 times smaller than the thickness of a sheet of paper [1]. The concept of nanotechnology was inspired by Richard Feynman's lecture "There is plenty of room at the bottom" [2]. In this talk, among other topics, he mentioned the possibility of substances with properties on the small scale that are very different to those in the bulk. Advances in fabrication techniques such as lithography and colloidal chemistry allowed for the production of nanoparticles that exhibit examples of this; e.g. increased reactivity due to an increase in surface to volume ratio [3] and superparamagnetism due to the fabrication of particles so small that they consist of a single magnetic domain [4]. Another of these properties that is unique to (metal) nanoparticles is localized surface plasmon resonance (LSPR) and it has been shown that this property can be utilized to measure changes in properties such as the thickness and refractive index of a layer of a substance in nanometer scale [5] [6] [7].

## *Localized Surface Plasmon Resonance*

Surface plasmons are the oscillations of conduction electrons that occur at the interface of two materials. This is most commonly seen at the surface of metals interfaced with a dielectric. These oscillations can be excited by light waves in certain conditions. When this occurs in nanoparticles that are of a size comparable to the wavelength of the incident light they are termed localized surface plasmons (LSP). The frequency at which maximum absorption for a particle occurs is called the localized surface plasmon resonance (LSPR) frequency for that particle and this will be discussed in more detail in the *Theory* section. For metal nanoparticles such as gold and silver this frequency is mostly within the visible spectrum. As a result, these particles, whether in colloidal solution or deposited on a clear surface, will appear to have a colour which is not usually associated with the corresponding metal. Also, this colour can change if the LSPR frequency changes, which depends not only on the size, shape and composition of a particle but also on the refractive index of the dielectric medium in the immediate vicinity of the particle. This is where its use in sensing stems from. The reason for this will also be examined in the *Theory* section.

While localized surface plasmons are a relatively recent discovery, the foundation for their revelation being in 1908 when Gustav Mie solved Maxwell's equations to describe the interaction of light with nanoparticles [8], their properties have been used for hundreds of years.

For example, many of the stained glass windows of churches and cathedrals around the world were, and still are, fabricated using plasmonic metal particles for over a thousand years. These particles were used to produce the vibrant colours that this type of window is famous for (Figure 1) [9] [10].



Figure 1. A 13th century stained glass window, from Chartres cathedral, produced using nanoparticles utilizing the properties of LSPR.

### *Nanoplasmonic Sensing*

In recent years, the properties of LSPR have been harnessed for more practical purposes, namely in the field of sensing, or *nanoplasmonic sensing*. There are companies, such as LamdaGen and Insplorion, which produce a range of specialised nanoplasmonic sensing devices. However, the most universally recognizable nanoplasmonic sensor is not a complicated or expensive instrument, it is the simple home pregnancy test.

As with the majority of successful and robust biosensors, the nanoplasmonic-based pregnancy test's mode of operation is relatively simple [11]. In the early stages of pregnancy, the body produces human chorionic gonadotropin hormone (hCG). This is what the biosensor is designed to detect. It does so through a combination of antibodies and gold nanoparticles. There are two sets of the antibodies, one set is bound to gold nanoparticles which are free to move along chromatography paper and the secondary set of antibodies are bound to the paper at an area called the sensing strip. When urine is introduced to the paper it travels laterally via capillary action, while doing so it also transports the antibody-gold nanoparticle complexes. If hCG is present it binds to these antibodies. When these gold-antibody-hCG complexes reach the sensing strip, the hCG in the complex binds to the secondary antibodies, resulting in the gold nanoparticles agglomerating in this area. Due to the close proximity of the particles, they have a screening effect on each other's LSPR frequency and this produces a bright red colour, indicating a positive test. Beyond the sensing strip there is a control strip. This consists of hormones similar to hCG that are adsorbed to the paper. Any gold-antibody complexes which have not bonded with hCG will attach here. The primary reason for this strip is to indicate test completion, especially in the case of negative tests. Similar devices using gold nanoparticles

have been adapted to detect a range of hormones, antigens and proteins to diagnose various medical conditions, such as prostate cancer [12], heart attack [13] and hepatitis B [14]. A schematic of the mode of operation of shown below (Figure 2).

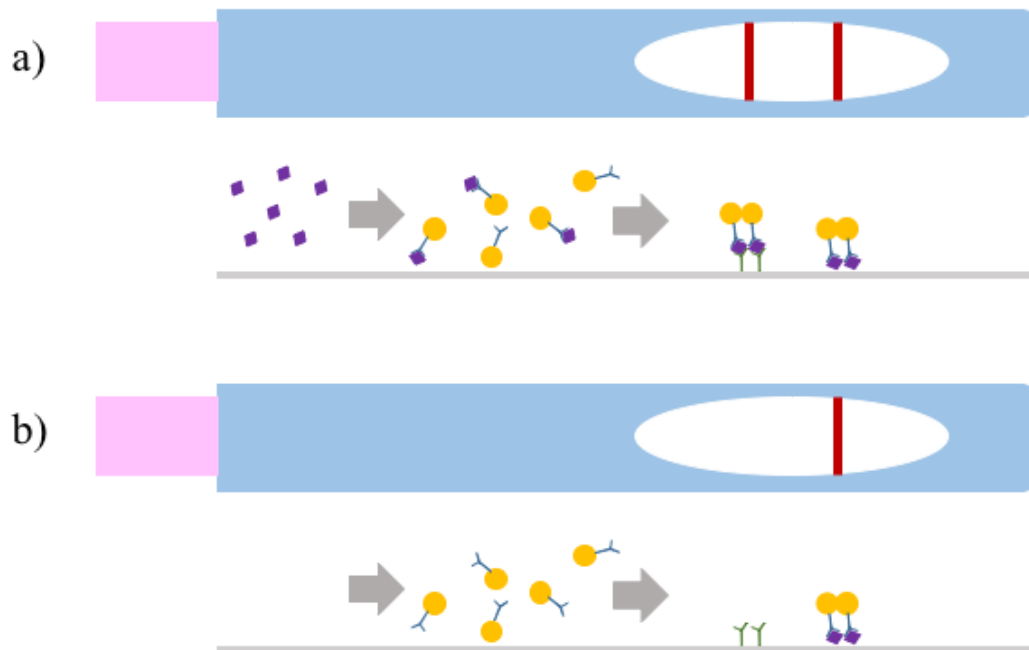


*Figure 2. Schematic showing the mode of operation for a nanoplasmonic home pregnancy test. (a) An example of a positive test. hCG, present in the urine of a pregnant user, binds to antibodies attached to gold nanoparticles. These subsequently bind to secondary antibodies adsorbed to the paper. (b) Due to the lack of hCG, in the case of a non-pregnant user, there is no binding at the sensing strip. The particles will still bind at the control strip, indicating that the sensor is functional and the test completed.*

Over the last decade, research into nanoplasmonics for biosensing has led to the development of very interesting techniques with the capability to reveal information at a biomolecular level. For example, similar to the mechanism utilized for the pregnancy test, gold nanoparticles modified with strands of DNA in solution have been used to measure sequence specific interactions between proteins and double stranded DNA [15]. It has also been found that nanopores surrounded by a gold film that facilitates SPR can be used to measure molecular binding kinetics to a lipid bilayer on the surface of the surface of this film [16]. A change in the SPR frequency is the mode of detection in this case. This is relatively similar to the mode of detection for the sensors produced in this project. Furthermore, the sensors produced in this project can also be used to detect changes upon the surface and within the structure of a lipid bilayer. This is important because cell membranes are composed of lipid bilayers. A multitude of biological processes are carried out via this membrane, such as cell signalling and cell adhesion, many of which involve molecular binding to the surface of this bilayer and/or conformational changes of molecules attached to the surface or of the bilayer itself. The ability to investigate such membrane processes, and to do so in real time, would be very exciting and potentially of vital importance.

## *Project Aim*

The aim of this project is to produce a nanoplasmonic ruler that can facilitate non-destructive measurements on a layer of material with nanometer resolution by utilizing the properties of LSPR. Unlike the sensors described in the previous section, this ruler is not selective, i.e. there is no use of antibodies. The ruler's functionality relies solely on changes in the properties of the dielectric medium surrounding the nanoantennas. Similar systems that utilize LSPR in this manner often consist of only one type of nanoantenna (same dimensions, chemical composition, shape, etc.) [17] [18] [19]. This can be problematic sometimes because only one unknown can be obtained, the thickness or refractive index of a layer of material, for example, both of which are often unknown in many scenarios prior to measurement. This can be overcome by adding an extra parameter that can be measured, i.e. two parameters enabling the calculation of two unknowns. A previous example of dual-parametric LSPR is the combination of LSPR and quartz crystal microbalance with dissipation [20], which enables the determination of protein uptake by a single lipid bilayer where the only required information is the protein density. The technique adopted in this project is somewhat less complicated in that both parameters are encapsulated within the design of a single sensor and all the data acquisition is solely from LSPR responses.

The project is a continuation of previous work carried out by the supervisor of this project, Ferry Nugroho. The aim is to use two types of nanoantennas of different dimensions in the fabrication of the device itself. Since the magnitude of the effect of the dielectric medium on the LSPR frequency of the nanoantennas is different depending on the dimensions of the nanoantennas, this could enable the simultaneous measurement of the thickness and refractive index of a layer of unknown composition. It could also detect changes to these values, with a view to use this as a means to analyze dynamic processes on the surface of this ruler. A major part of this project will focus on producing this ruler with a flat surface. The vast majority of nanoplasmonic devices (devices that utilise LSPR) consist of nanoantennas sitting upon a surface [7] [17] [18] [21]. For many samples, primarily in the biosensing field, the presence of topographical variations such as those produced by protruding nanoantennas can have an effect on measurements [22]. By using techniques similar to those developed by Nugroho et al. [22], the objective is to produce a topographically flat dual-nanoantenna nanoplasmonic ruler.

## 2. Theory

### *Plasmons and their interaction with light*

In metals, there exists a large number of free roaming conduction electrons. These can be viewed as a negatively charged electron gas that is spread out and moving around the positively charged lattice structure of the metal. Any collective movement of electrons will result in a restorative Coulomb force being exerted by the lattice on the electrons. Much like a pendulum swinging under the restorative force of gravity, electrons tend to overshoot the source of this force, leading to oscillations known as plasma oscillations or Langmuir waves. The frequency at which these oscillations occur is termed the plasma frequency,  $\omega_p$ ,

$$\omega_p = \sqrt{\frac{Ne^2}{m_e \epsilon_0}} \quad (2.1)$$

where  $N$  is the number of oscillating electrons,  $\epsilon_0$  is the permittivity of free space,  $m_e$  is electron mass and  $e$  is the elementary charge. Plasmons are the quantizations of these oscillations.

Electric fields, such as those produced by a photon, can excite these oscillations. The motion of an electron moving through such a field can be described by the following equation [23]

$$m_e \frac{\partial^2 \mathbf{r}}{\partial t^2} + m_e \Gamma \frac{\partial \mathbf{r}}{\partial t} + m_e \omega_0^2 \mathbf{r} = -e\mathbf{E}(\mathbf{r}, t) \quad (2.2)$$

where  $\mathbf{r}$  is the displacement of the electron from equilibrium,  $\Gamma$  is dampening due to scattering off other electrons and the lattice,  $\omega_0$  is the natural frequency of the restoring force exerted on an electron bound to an atom and  $\mathbf{E}$  is the net field acting on the electron. The left hand side of the equation essentially consists of the acceleration force, the frictional force and the restorative force.

The way in which light, or any external electric field, interacts with metals is affected by the frequency of the field and plasma frequency of the metal. The nature of this relationship will now be derived. Firstly, the displacement of an electron in a metal by an external field, expressed in the frequency domain, is found through the Fourier transform of equation 2.2,

$$\begin{aligned} m_e(-i\omega)^2 \mathbf{r}(\omega) + m_e \Gamma(-i\omega) \mathbf{r}(\omega) + m_e \omega_0^2 \mathbf{r}(\omega) &= -e\mathbf{E}(\omega) \\ \Rightarrow (-m_e \omega^2 - m_e \Gamma i\omega + m_e \omega_0^2) \mathbf{r}(\omega) &= -e\mathbf{E}(\omega) \\ \mathbf{r}(\omega) &= -\frac{e}{m_e \omega_0^2 - \omega^2 - \Gamma i\omega} \mathbf{E}(\omega) \end{aligned} \quad (2.3)$$

The electrical dipole moment,  $\boldsymbol{\mu}(\omega)$ , which is a measure of the separation of two opposite charges in the material is given by

$$\boldsymbol{\mu}(\omega) = -e\mathbf{r}(\omega) \quad (2.4)$$

By inserting (2.3) into (2.4)

$$\boldsymbol{\mu}(\omega) = \frac{e^2}{m_e} \frac{\mathbf{E}(\omega)}{\omega_0^2 - \omega^2 - \Gamma i \omega} \quad (2.5)$$

Polarizability,  $\alpha$ , which is a measure of a material's ability to form dipoles is defined by

$$\begin{aligned} \alpha(\omega) &= \frac{\mathbf{E}(\omega)}{\boldsymbol{\mu}(\omega)} \\ \Rightarrow \boldsymbol{\mu}(\omega) &= \alpha(\omega) \mathbf{E}(\omega) \end{aligned} \quad (2.6)$$

Therefore, from (2.5) and (2.6)

$$\alpha(\omega) = \frac{e^2}{m_e} \frac{1}{\omega_0^2 - \omega^2 - \Gamma i \omega} \quad (2.7)$$

The total polarization of a material per unit volume,  $\mathbf{P}$ , is given by

$$\mathbf{P}(\omega) = N \boldsymbol{\mu}(\omega) \quad (2.8)$$

where  $N$  is the number of dipoles per unit volume. For simplicity, it is assumed that these dipoles do not affect one another.

$\mathbf{P}$  can also be stated in terms of electric susceptibility,  $\chi$ , which is a dimensionless proportionality constant that indicates the amount of polarization induced in a material under the influence of an electric field

$$\mathbf{P}(\omega) = \varepsilon_0 \chi(\omega) \mathbf{E}(\omega) \quad (2.9)$$

By combining (2.6), (2.7), (2.8) and (2.9)

$$\begin{aligned} \chi(\omega) &= \frac{N \alpha(\omega)}{\varepsilon_0} \\ \Rightarrow \chi(\omega) &= \frac{N e^2}{\varepsilon_0 m_e} \frac{1}{\omega_0^2 - \omega^2 - \Gamma i \omega} \end{aligned} \quad (2.10)$$

By inserting (2.1) into (2.10)

$$\chi(\omega) = \frac{\omega_p^2}{\omega_0^2 - \omega^2 - \Gamma i \omega} \quad (2.11)$$

The susceptibility of a material is related to the relative permittivity of the material,  $\varepsilon_r$ , by

$$\chi = \varepsilon_r - 1 \quad (2.12)$$

Permittivity is an important property when discussing electric fields and their interactions with materials. Basically, it is a measure of how an external electric field affects a medium but also how this medium affects the field. It can be viewed as a measure of the reduction of an electrical field in a medium. Relative permittivity is the ratio of the permittivity and the permittivity of free space,  $\epsilon_0$ , and is related to refractive index,  $n = \sqrt{\epsilon_r}$ .

By inserting (2.12) into (2.11)

$$\epsilon_r = 1 + \frac{\omega_p^2}{\omega_0^2 - \omega^2 - \Gamma i \omega} \quad (2.13)$$

As mentioned previously, the electrons that oscillate in metals are the conduction electrons, which are not bound to atoms. Therefore,  $\omega_0 = 0$  for metals.

(2.13) simplifies to

$$\epsilon_r = 1 - \frac{\omega_p^2}{\omega^2 + \Gamma i \omega} \quad (2.14)$$

Permittivity is a complex valued parameter which means that equation 2.14 can be further split into its real and imaginary components.

$$\begin{aligned} \epsilon_r &= \epsilon_r' + \epsilon_r'' \\ &= 1 - \frac{\omega_p^2}{\omega^2 + \Gamma i \omega} \frac{\omega^2 - \Gamma i \omega}{\omega^2 - \Gamma i \omega} \\ &= 1 - \omega_p^2 \frac{\omega^2}{\omega^4 + \Gamma \omega^2} + i \omega_p^2 \frac{\Gamma \omega}{\omega^4 + \Gamma \omega^2} \end{aligned} \quad (2.15)$$

Simplifying and separating (2.15)

$$\epsilon_r' = 1 - \frac{\omega_p^2}{\omega^2 + \Gamma^2} \quad (2.16)$$

$$\epsilon_r'' = \frac{\omega_p^2 \Gamma}{\omega^3 + \Gamma^2 \omega} \quad (2.17)$$

Since the interest of plasmonics is primarily in the visible light range,  $\omega \gg \Gamma$ . For example, for silver,  $\Gamma = 5.5 \times 10^{12}$  Hz [24], whereas for the visible light range  $\omega = 3.99 \times 10^{14} - 7.5 \times 10^{14}$  Hz. Therefore, equations 2.16 and 2.17 can be further simplified

$$\epsilon_r' = 1 - \frac{\omega_p^2}{\omega^2} \quad (2.18)$$

$$\epsilon_r'' = \frac{\omega_p^2 \Gamma}{\omega^3} \quad (2.19)$$

As can be seen with equation 2.18, when the frequency of an external electric field,  $\omega$ , approaches the plasma frequency,  $\omega_p$ ,  $\epsilon_r'$  approaches zero. It is at this point that collective oscillation of the electrons occurs. This collective oscillation is sustained as long as the external field is maintained at a frequency that is equal to the plasma frequency,  $\omega_p$ . Conceptually, this can be compared to a child on a swing that is being pushed by a friend. The swing moves at a frequency that is dependent only on the length of the rope that attaches the swing to its frame. If the friend applies a pushing force at a frequency that is equal to the swing's frequency, the child will swing in a constant fashion. If the friend stops applying this force or changes the frequency of the pushing force, the oscillations will stop or be disrupted.

When  $\omega > \omega_p$ , the electrons in a material do not move fast enough to screen the incoming field, resulting in transmission of the field. Whereas, when  $\omega < \omega_p$ , the electrons can follow the electric field, screening it and resulting in reflection of the field. Since the plasma frequency for most metals is  $\sim 1.93 \times 10^{15} - 2.42 \times 10^{15}$  Hz [24], which is significantly larger than the frequency range for visible light, which lies between  $3.99 \times 10^{14}$  to  $7.5 \times 10^{14}$  Hz, most metals appear reflective and shiny.

### *Localized Surface Plasma Resonance*

As mentioned in the introduction, properties at the nanoscale often differ from those at the bulk scale, as is the case for plasmons in nanoparticles. Unlike the bulk material, for metal particles smaller than the wavelength of visible light, all of the free electrons collectively oscillate when the plasmon resonance frequency conditions are met. These oscillations are obviously confined to the volume of the particle, leading to the name *localized* surface plasmon resonance. Also, due to the increased concentration of surface electrons, light can couple with these surface plasmons.

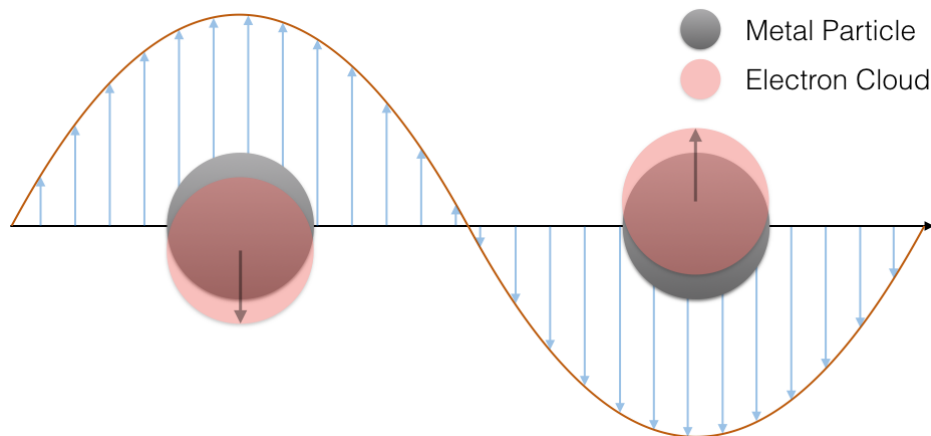


*Figure 3. A schematic illustrating localized surface plasmon resonance excitation of a nanoparticle by electromagnetic radiation. As the particle is subjected to an external electric field, the conduction electrons, represented as an electron cloud above, are pushed out of equilibrium. A restoring force from the unmoved positive nuclei draw the electrons back towards the equilibrium position. When the particle is subjected to a field with a frequency that is equal to the LSPR frequency for that particle, collective and coherent oscillation of the conduction electrons is maintained.*

Plasmon excitation decays one of two ways, either by electron-hole excitation or by radiation. It is this decay that results in the large amount of absorption and scattering of light at the plasmon frequency. Light that enters the electron-hole excitation decay channel is absorbed by the particle. Light that enters the second channel is said to be scattered. This is due to the fact that light at the resonance frequency causes a dipole oscillation which will itself re-radiate. This is an example of Rayleigh scattering.

The extent to which a particle scatters and/or absorbs light is defined in a parameter known as scattering or absorption cross section. The addition of these gives the extinction cross section. The equations for the calculation of these parameters are shown below.

$$\sigma_{abs} = kIm(\alpha) \quad (2.20)$$

$$\sigma_{sca} = \frac{k^4}{6\pi} |\alpha|^2 \quad (2.21)$$

$$\sigma_{ext} = \sigma_{abs} + \sigma_{sca} \quad (2.22)$$

where  $\alpha$  is the material polarizability and  $k$  is the wave vector.

As might be expected, for non-transparent particles that do not interact with light the extinction cross section is equal to the geometric cross section of the particles. For particles that do interact with light, such as the metal nanoparticles previously mentioned, the extinction cross section is dependent on the frequency of the light. At the LSPR frequency,  $\alpha$  is at its maximum (discussed more in the next section), therefore, the extinction cross section is also at its maximum and is actually greater than the particle's geometric cross section. This is the reason for the characteristic bright colours associated with metal nanoparticles.

### *LSPR for biosensing*

In order for LSPR to be useful for biosensing, there must exist a measurable relationship between the nanoparticles and the medium surrounding these particles. This relationship is found to be the relative permittivity of the surrounding medium and the measured LSPR frequency of the particles. The equations in this section are primarily from ref [25]. When discussing the relationship between the measured LSPR frequency and the relative permittivity of the surrounding medium it is both necessary and practical to use the applied electric field,  $\mathbf{E}_0$ , instead of the net field,  $\mathbf{E}$ , that was used in the previous sections. However, both are related by

$$\mathbf{E} = \frac{\mathbf{E}_0}{\epsilon_r} \quad (2.23)$$

For a bulk sample of a metal, substituting (2.23) and (2.12) into (2.9) gives

$$\mathbf{P} = \epsilon_0(\epsilon_r - 1) \frac{\mathbf{E}_0}{\epsilon_r} \quad (2.24)$$

If defined in a similar way to (2.6)

$$\mathbf{P} = \alpha \mathbf{E}_0 \quad (2.25)$$

Therefore

$$\alpha = \frac{\varepsilon_0(\varepsilon_r - 1)}{\varepsilon_r} \quad (2.26)$$

When the frequency of the net electric field is equal to the plasmon resonance frequency,  $\varepsilon_r$  is equal to zero, as shown by equation 2.18. This also implies that the resonance condition is met whenever the denominator in the polarizability of a material approaches zero. This is logical since polarizability would be at a maximum. At this point the ease at which the electrons can oscillate is at its greatest.

For a particle surrounded by a medium, the particle's polarizability, which is eloquently derived in [25], is described as

$$\alpha = V \frac{\varepsilon_0 \varepsilon_1 (\varepsilon_2 - \varepsilon_1)}{[\varepsilon_1 + L(\varepsilon_2 - \varepsilon_1)]} \quad (2.27)$$

where  $V$  is the volume of the particle,  $\varepsilon_2$  is the relative permittivity of the particle,  $\varepsilon_1$  is the relative permittivity of the medium surrounding the particle and  $L$  is a shaping factor ( $L = 1$  for a slab of material and  $L = 1/3$  for a sphere). Again, if it is assumed that the resonance condition is met when the denominator for the polarizability approaches zero, and that the particle in this case is a sphere, resonance occurs when

$$\varepsilon_2 = -2\varepsilon_1 \quad (2.28)$$

For most samples of interest in biosensing,  $\varepsilon_1$  is real and positive. This introduces a condition on  $\varepsilon_2$  which must have a negative real part and a small imaginary part, which is the case for many of the metals used in nanoplasmonic sensing.

Assuming a negligible imaginary part, (2.28) can be substituted into (2.18)

$$\begin{aligned} -2\varepsilon_1 &= 1 - \frac{\omega_p^2}{\omega^2} \\ \Rightarrow \omega_{LSPR} &= \frac{\omega_p}{\sqrt{1 + 2\varepsilon_1}} \end{aligned} \quad (2.29)$$

where  $\omega_p$  is the plasma frequency for the bulk material the particle is made of and  $\omega_{LSPR}$  is the measured LSPR. This introduces a direct relationship between the particle's LSPR and the medium surrounding the particle.

To summarize, the extinction cross section of a nanoparticle is directly related to its polarizability. This polarizability is dependent on a number of factors but, most importantly for biosensing, one of these is the permittivity of the medium surrounding the particle (or particles, as is the case for most nanoplasmonic biosensors). This permittivity is inversely proportional to the LSPR frequency. The LSPR frequency can be detected using a spectrometer as the frequency where extinction by the particle(s) is the highest. Any change in the surrounding medium will be detected as a change in frequency (or wavelength) of the maximum extinction peak, as illustrated by Figure 4.

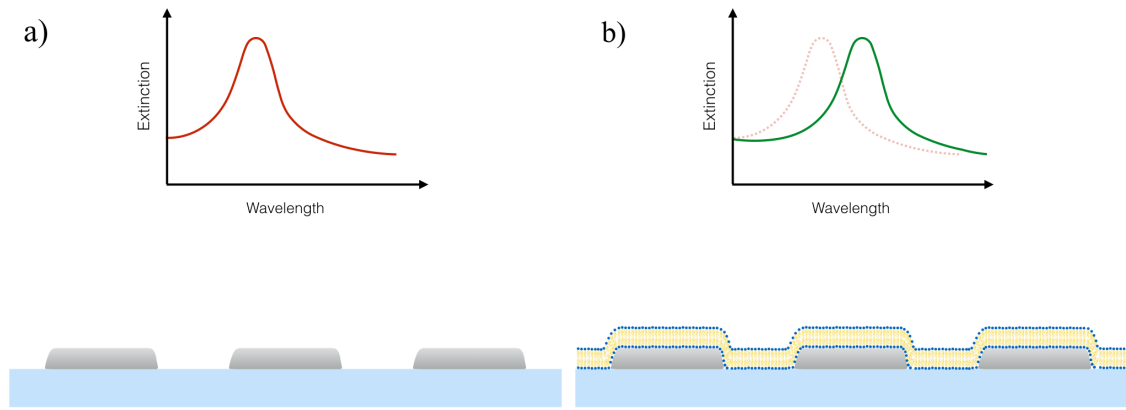


Figure 4. A schematic showing the LSPR shift upon a change in the medium surrounding nanoplasmonic particles. Although frequency has been used in this report when discussing LSPR, all measurements were actually carried out in terms of wavelength. Wavelength is inversely proportional to frequency. a) An example of the LSPR peak for a nanoplasmonic sensor consisting of silver nanodisks on a glass substrate. b) As a lipid bilayer forms upon the silver nanodisks, a change in the permittivity surrounding the nanodisks results in a shift of the LSPR wavelength, from the red dotted spectrum to the new green spectrum.

The general relationship between the LSPR frequency and the plasma frequency can be determined by making  $\epsilon_1 = 1$  (relative permittivity of a vacuum).

(2.29) then becomes

$$\omega_{LSPR} = \frac{\omega_p}{\sqrt{3}} \quad (2.30)$$

From equation 2.30, it can be seen that  $\omega_{LSPR}$  is lower than  $\omega_p$ . This also helps to explain why metallic nanoparticles tend to be colourful whereas bulk metals are shiny and reflective. As mentioned previously,  $\omega_p$  tends to be in the UV region, whereas, due to the colourful nature of metallic nanoparticles,  $\omega_{LSPR}$  must be in the UV-vis regime. Equation 2.30 would be in agreement with this.

### Dual-sized nanoantennas

As shown in Figure 4, a change in the refractive index (or relative permittivity) in the region surrounding a nanoplasmonic particle causes a shift in the LSPR wavelength for this particle. The region wherein a change in refractive index is detectable is called the decay length for a given particle, which is proportional to the size of this particle and exponentially vanishes. Essentially, the particle detects a change in the effective refractive index of the entire region within the decay length. If the decay length for a particle is known, and the refractive index of a film that forms on the particle is also known, it is possible to calculate the thickness of the film,  $d_f$ , by using [26]

$$d_f = \ln \left( 1 - \frac{R}{S(n_f - n_b)} \right) \delta \quad (2.31)$$

where  $R$  is the peak shift of the LSPR wavelength upon adsorption of the film,  $n_f$  and  $n_b$  are the refractive index of the film and the surrounding medium (usually water), respectively,  $\delta$  is the decay length and  $S$  is the sensitivity factor, which is determined before each measurement and expressed as LSPR wavelength shift per change in bulk refractive index unit.

In many situations, such as with complex biological samples, the refractive index is not known. This problem is solved with dual-parametric sensors. Previous papers have used dual-parameters such as dual-wavelength with varying angles of incidence to excite surface plasmon resonance (SPR) on a gold film [27] or nanoplasmonic sensing combined with quartz crystal microbalance (QCM) sensing [20]. The theory behind these techniques is that each parameter is affected by the medium surrounding the sensor in a different way. For example, in ref [20], the mass of the adsorbed film could be determined by the QCM. If any change in the refractive index was detected by the nanoplasmonic disks used in this paper but no change in mass was detected by the QCM it could be deduced that the change in refractive index was due to a conformational change within the film at the surface and not a change in the film's overall thickness. It is not possible to obtain this type of in-depth information using a standard nanoplasmonic sensor consisting of identical disks.

Ref [27] is based on the fact that SPR along a thin metal film is excited by light depending angle of incidence of the light. SPR conditions are met when the intensity of the light reflected off the metal film is at a minimum, which can easily be measured. A change in the SPR frequency results in a shift in the angle at which this occurs, this shift is known as the SPR sensor response. Several of the physical parameters that determine this response are wavelength dependent, this is the reason why the dual-wavelength technique can be used. By measuring the ratio of the response for both wavelengths it was possible for the researchers to obtain the thickness of a film directly from this. A similar technique is used for this project.

By using a dual-sized nanoantenna system it is possible to obtain two LSPR sensor responses to a change in the refractive index around the antennas. This is due to the fact that, as mentioned before, the LSPR wavelength depends on the size of a particle. The magnitude of the LSPR response also depends on this.

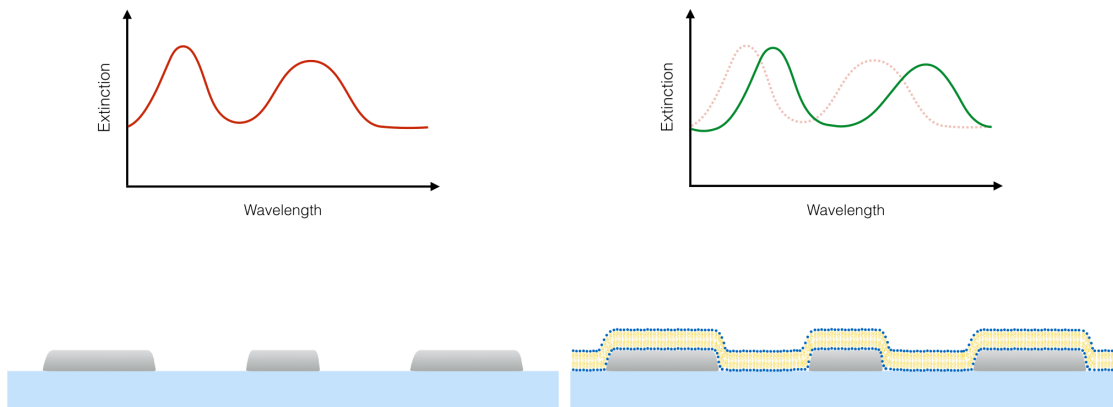


*Figure 5. A schematic showing the LSPR sensor response for a dual-sized nanoantenna sensor. The ratio of the shift for each peak can be used to directly calculate the thickness of a film.*

By rearranging (2.31)

$$R_i = S(n_f - n_b)\varphi_i \quad (2.32)$$

And by adapting the same ratio technique as that used in [27]

$$\begin{aligned} \frac{R_1}{R_2} &= \frac{S_1(n_f - n_b)[1 - e^{-d_f/\delta_1}]}{S_2(n_f - n_b)[1 - e^{-d_f/\delta_2}]} \\ \Rightarrow \frac{R_1}{R_2} &= \frac{S_1}{S_2} \frac{1 - e^{-d_f/\delta_1}}{1 - e^{-d_f/\delta_2}} \end{aligned} \quad (2.33)$$

From this, if  $S$  and  $\delta$  are known, it is possible to plot the ratio of the peak shift for each antenna versus the thickness of the film adsorbed to the surface. The sensitivity factor,  $S$ , is measured via bulk refractive index sensitivity measurements and the decay length,  $\delta$ , is calculated using equation 2.32 with a film of a known thickness and refractive index. These techniques will be discussed in more detail in the *Method* section.

After the ratio is experimentally measured and the film thickness obtained from the aforementioned plot, the refractive index can be calculated by rearranging equation 2.31

$$n_f = \frac{\left(\frac{R_i}{1 - e^{-d_f/\delta_i}}\right)}{S_i} + n_b \quad (2.34)$$

### 3. Fabrication

The complete fabrication of a topographically flat dual-sized nanoantennas sensor chip was a 3 step process:

1. Fabrication of the nanoplasmonic antennas on glass was carried out using hole-mask colloidal lithography [28]
2. These antennas were then embedded in silicon dioxide or silicon nitride via plasma enhanced chemical vapour deposition (PECVD)
3. This dielectric layer was milled using ion beam milling (IBM) to achieve a flat surface

#### *Hole-mask colloidal lithography [28]*

Hole-mask colloidal lithography (HCL) is an example of a bottom-up technique of nanofabrication. It is termed “bottom-up” since it relies on the self-assembly of small particles in order to produce a desired structure, i.e building from the bottom up. In the case of HCL, it is colloidal polystyrene (PS) beads that self-assemble on a surface that leads to the fabrication of an evaporation mask through which material can be deposited. The main steps in the HCL process are as follows:

- I. Substrate cleaning
- II. Spin coating
- III. Particle dispersion
- IV. Mask deposition
- V. Particle stripping
- VI. Reactive ion etching
- VII. Material deposition
- VIII. Lift-off

Where relevant, many of the following subsections contain general information on each process followed by information specific to this project.

#### I. Substrate cleaning

As with all nanofabrication processes, it is imperative to ensure that all surfaces are clean prior to, and during, fabrication. The substrates used in this project were glass and silicon. Glass was used for the device itself and silicon for investigation with SEM, which will be discussed further in the *Characterisation* section. First, the substrates were placed in a beaker with acetone and sonicated for 3 minutes. This process was then repeated for isopropanol (IPA), followed by deionized water (DIW). After the water step, each substrate was thoroughly dried under nitrogen.

#### II. Spin coating

Spin coating is a technique by which one can deposit a thin layer of material evenly over a flat surface. This relatively simple method is used extensively in nanofabrication, primarily for the

application of resists to substrates. Resists are polymeric materials whose solubility properties change after exposure to radiation. In some cases, including for HCL, resists are not used because of this property but due to their overall stability and their solubility in specific solvents. A drop of solution is applied to a substrate which is then spun at an angular velocity which is high enough to force the drop to spread out evenly along the surface while also causing the solvent to evaporate. The substrate is then placed on a hot plate to evaporate any remaining solvent. The thickness of a deposited film depends on the viscosity of the solution and the angular velocity of the spinning. The relationship between these values can usually be obtained through the resist manufacturers in the form of spin speed curves.

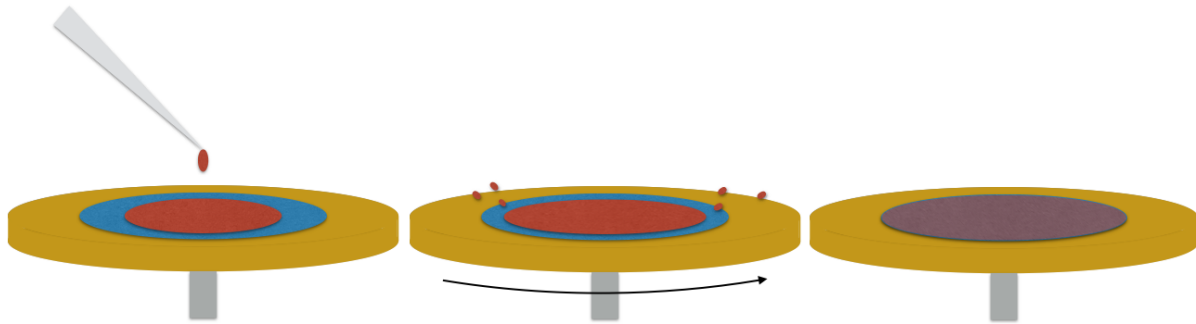


*Figure 6. A schematic showing the spin-coating process. From left to right: The resist is applied onto a substrate with a pipette followed by spinning which removes excess solution and evaporates solvent which results in a thin layer of resist upon the substrate.*

For this project, the resist that was used was poly(methyl methacrylate) (PMMA) (950 A4), which was spun at 2000 rpm for 1 minute. This was then baked on a hotplate for 5 minutes at 170°C. The thickness of the resulting PMMA layer was 250-300 nm [29]. Also, the substrates used for this particular project were in fact square in shape.

### III. Particle dispersion

As mentioned previously, the particles to be dispersed were PS beads which were in a colloidal mixture in MilliQ water. In order to produce the dual-sized antennas desired for this project a colloidal mixture containing PS beads of two different diameters was prepared.

Prior to PS bead dispersion it was necessary to prepare the surface of the substrate, which was PMMA at this time. PMMA is a hydrophobic material which is not ideal since dispersion requires full surface wetting. This problem was overcome by a short (5 s) reactive ion etching (RIE) with oxygen. RIE with oxygen increases surface energy due to reactions between the PMMA surface and oxygen but also introduces some surface roughness, both of which increase hydrophilicity [30]. RIE will be discussed on more detail later in this section. PS beads are negatively charged, therefore, after surface activation with RIE, a polyelectrolyte was applied to the surface of the substrate to produce a thin positively charged layer on the PMMA. The polyelectrolyte used was polydiallyldimethylammonium (PDDA), which was pipetted onto the surface until full surface coverage was achieved. This was left on the surface for 40 s, rinsed with DIW for 20 s and then dried under nitrogen.

At this stage the surface was ready for PS bead dispersion on the substrate surface. A pipette again was used to drop enough PS bead colloidal solution to wet the entire surface of the substrate. This was left for 3 min, rinsed for 20 s with DIW and dried thoroughly under nitrogen. It was necessary to dry thoroughly to prevent any possible particle agglomeration upon the surface.



Figure 7. A schematic showing the particle dispersion process. After the PMMA layer on the surface of the substrate is activated and charged by RIE with oxygen and PDDA, respectively, a pipette is used to apply a colloidal solution of PS beads. After rinsing and drying the PS beads remain on the surface.

#### IV. Mask deposition

E-beam physical vapour deposition (EBPVD) was used to deposit a thin metal film which would act as a mask for later depositions. In EBPVD, a bulk specimen of material, known as the source, is heated under high vacuum to a temperature high enough to cause evaporation of the material. This gaseous phase then travels to the substrate where it condenses, forming a thin layer. As the name suggests, for EBPVD the source is heated by an electron beam. Electrons, produced via thermionic emission or field electron emission are accelerated at high voltage towards the source, the direction of the beam is controlled by a magnetic field. EBPVD operates under high vacuum due to both the electron beam and the evaporated material. The presence of excess molecules could have adverse effects, such as attenuate and affect the direction of the electron beam, but also increase collisions of the evaporated material prior to deposition on the substrate, which could affect the uniformity of the deposited film. Controlling the accelerating voltage and current of the beam can be used to control the deposition rate which, in conjunction with a shutter mechanism, can control the thickness of the deposited film deposited on the substrate.

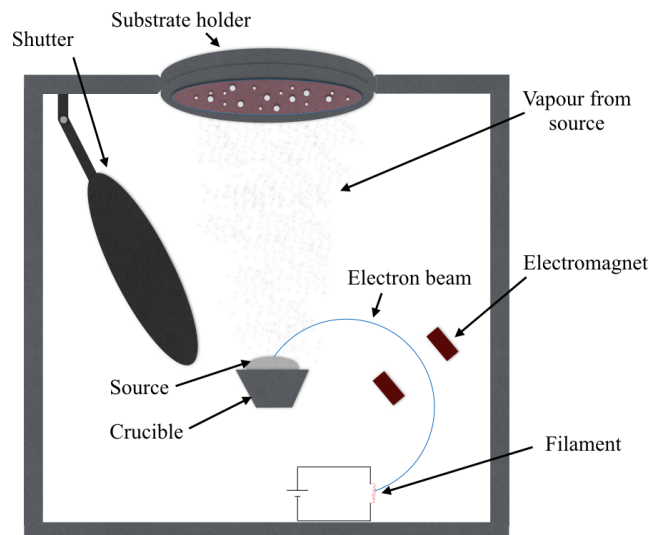


Figure 8. A schematic showing the main components of an EBPVD tool. The filament emits electrons which are accelerated at high voltage and directed by electromagnets towards a source contained in a crucible. The source becomes heated and starts to evaporate. This vapour condenses on the substrate on the substrate holder. After the desired thickness is achieved, deposition is stopped by a shutter mechanism.



Figure 9. The substrate after EBPVD. As shown here, the substrate and PS beads are completely covered by this process.

15 nm of chromium was deposited on top of the PMMA and PS beads using a Lesker EBPVD for this project.

#### V. Particle stripping

SWT-10 tape is used to strip away the PS beads under the thin metal film. As the beads are stripped away so too is the metal immediately above each bead, producing holes in the metal and forming a mask.

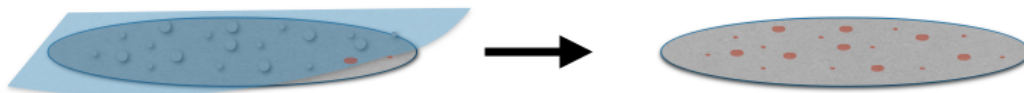
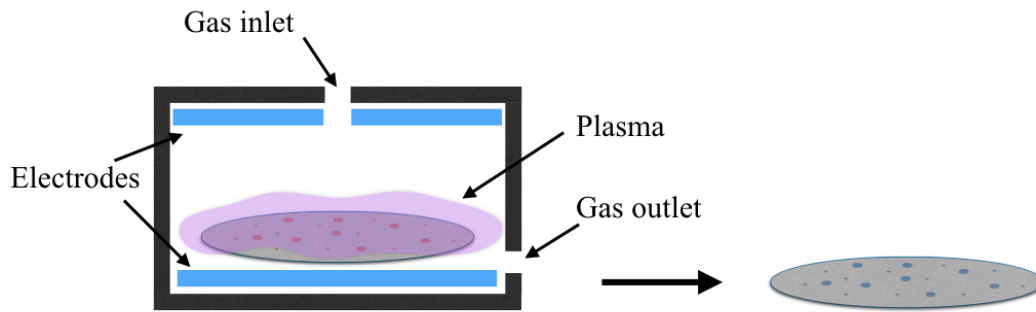


Figure 10. A schematic showing the tape-stripping process and the PMMA layer exposed through the holes produced in the chromium metal film by this technique.

Since two PS bead sizes were used for this project it was necessary to strip twice to ensure removal of all of the particles.

#### VI. Reactive ion etching

Reactive ion etching does what the name suggests, uses reactive ions to etch away certain materials. These ions are produced in a plasma chamber. A low vacuum is maintained in the chamber with a small volume of the etching gas of choice introduced to the chamber via an inlet valve. Plasma is formed when an oscillating electric field produced between two electrodes is strong enough to remove electrons from the etching gas, forming free electrons and highly reactive ions. When these electrons collide with the walls of the chamber they are grounded. However, when they collide with the substrate they introduce a negative charge. As this charge builds up, the positive ions are attracted to the substrate, a higher surface charge increasing the velocity of ions towards it. It is for this reason that RIE is both a physical and chemical form of dry etching. Unlike wet etching, which takes place in solution, RIE is highly anisotropic and reproducible.



*Figure 11. A schematic showing the main components in a RIE setup and the substrate after RIE treatment. Gas, oxygen in this case, is pumped into the inlet valve. An electric field produced by the two electrodes strips electrons from the oxygen, resulting in the formation of a plasma. Oxygen ions etch the PMMA layer through holes in the chromium, exposing the bare substrate underneath. The reactant products are removed via an outlet valve*

In subsection III, RIE was used to react oxygen with PMMA to increase surface energy and roughness by partially etching the PMMA. In this step the reaction time was increased to 5 minutes in order to etch away all of the PMMA which was exposed after tape stripping. Chromium is resistant to RIE with oxygen and therefore remains intact.

#### VII. Material deposition

At this stage the specimen consisted of a substrate with a layer of PMMA and chromium, both of which had holes in them produced by RIE and tape stripping, respectively. At this stage, material deposition was carried out by using the Lesker PVD described in subsection IV. Prior to the commencement of the project it was decided that silver would be the best material to use for the fabrication of the disks since the interband transition for silver lies outside of the analysis range of interest, facilitating the possibility the obtain maximum peak separation. 20 nm of silver was deposited.



*Figure 12. The substrate after deposition of silver via PVD*

#### VIII. Lift-off

Lift-off is the process by which a sacrificial layer of material is etched away by an etchant or solvent in order to remove other materials from the substrate.

PMMA was the sacrificial layer in this project. Acetone was used to dissolve the PMMA which resulted in the “lift-off” of the chromium mask and excess silver. The resulting specimen was rinsed with IPA and dried under nitrogen.

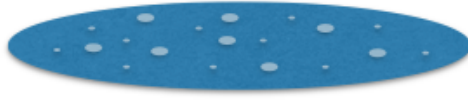


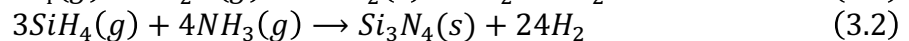
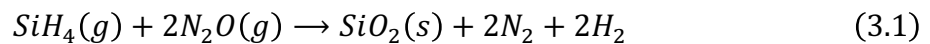
Figure 13. The final product after lift-off. This consisted of dual-sized nanodisks with a height of 20 nm on glass (or silicon).

### *Plasma enhanced chemical vapour deposition*

At this stage of the fabrication, the disks were embedded in a thin layer of silicon oxide or silicon nitride. There were a number of reasons for this. First and foremost, silver, which the disks were made of, is relatively susceptible to oxidation when in nanoparticle form. Embedding the disks could protect against this. Also, to produce a topographically flat chip it was obviously necessary to add a layer of material in order for the surface of the sensor to be altered without affecting the disks themselves. Finally, this process should also produce a surface with a uniformed chemical composition that is unreactive with biological samples.

Chemical vapour deposition (CVD) is a technique wherein gaseous reactants are encouraged to react on the surface of a substrate to produce a thin film. This is accomplished by applying heat to the substrate that will, in turn, supply the activation energy needed for the reaction to occur to produce the film. In many cases this energy can be quite high which would require heating to a temperature that is not compatible with the given substrate. This can be overcome by the use of plasma. PECVD uses an electric field to ionise the reactants which decreases the activation energy, i.e the substrate temperature, needed to produce the reaction products on the substrate surface. As you may recall, this process is almost identical to the RIE system mentioned in the previous section. The main differences between the two systems are that PECVD requires the application of heat and, in many cases, a load lock. This load lock is necessary due to both the low pressure used in the reaction chamber and the use of silane gas as the silicon source, which is extremely flammable and pyrophoric (ignites spontaneously in air).

The basic reactions of the gases used for the PECVD process in this project for the production of silicon dioxide and silicon nitride films were



The deposition rate increases as the partial pressures of the reactants in the chamber increases, the temperature of the substrate increases and/or the distance between the electrodes and the substrate decreases [31]. Increasing the field power initially leads to an increase in the deposition rate, due to an increase in the concentration of reactive ions. However, beyond a certain power, any further increase does not increase deposition rate. This may be due to process inhibition by ion bombardment and/or plasma-etching processes at high field power [32]. The final film thickness is determined by the deposition time.

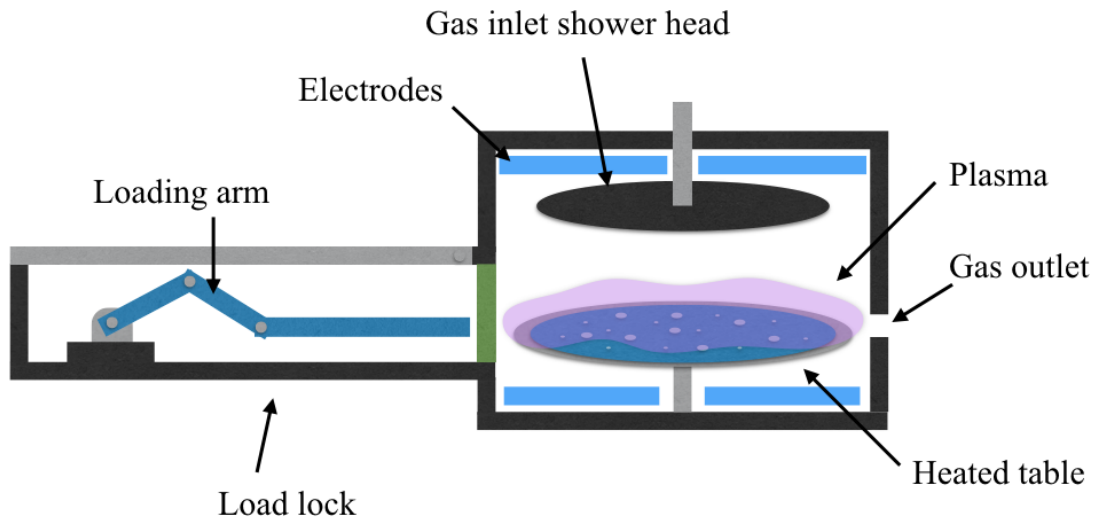


Figure 14. A schematic showing the main components of a PECVD system. The substrate is loaded into the chamber via the load lock using the loading arm. Reactants are directed towards the surface of the substrate from a heated gas inlet shower head. Prior to reaching the substrate, the reactants are ionised by an electric field between two electrodes. These ionised reactants then combine to form a thin film on the substrate (as well as elsewhere in the chamber). The by-products are pumped out via the gas outlet.

For this project, 10 nm of silicon dioxide or silicon nitride were used to embed the nanoantennas, resulting in corrugated chips. Silicon dioxide was investigated due to its well documented use in biological adsorption measurements [33] [34] [35] and silicon nitride was investigated due to its apparent superior stability to silicon dioxide as an embedding material for silver nanoparticles as experienced by the group in previous projects. For the purposes of milling, a thicker oxide layer was needed. This was due to the fact that as milling with optimised parameters proceeded, the roughness of the surface decreases along with the thickness of the oxide. It was decided that 100 nm of silicon dioxide upon the dual-sized nanoantennas would most likely be sufficient to produce a flat surface when the targeted final oxide thickness was reached using this technique. Silicon nitride was also used for the milling step but due to differing milling rates for silicon nitride and silicon dioxide and a lack of time to investigate both materials extensively, it was decided to focus on optimising the milling parameters for silicon dioxide.



Figure 15. A chip consisting of dual-sized nanoantennas embedded in 100 nm of silicon dioxide.

## *Ion beam milling*

Ion beam milling, also called ion beam etching (IBE), uses high energy ions to remove unwanted material from a sample. IBE can be used to obtain fast, anisotropic and reproducible etching. Also, the duration of etching can be controlled exactly, which is practically impossible with wet etching. When compared with RIE, which is similar in many ways, the two main differences are that the angle of milling/etching can easily be controlled with IBE, leading to a higher quality of anisotropic etching, and that the ions used in IBE do not react with the sample during the etching process. Etching is solely a physical process in regards to IBE.

In most cases, the ions used in IBE are argon ions which are created by a Kaufman ion source. Atoms of argon are ionised in a discharge chamber by electrons that are introduced via a filament. These electrons are confined to a specific region by a magnetic field. When these electrons bombard an argon atom it can lose an electron of its own, creating a positively charged argon ion and a free electron, which will increase the concentration of free electrons in the chamber and increase ionisation. Excess electrons are collected by an anode which mitigates the build-up of charge in the discharge chamber. A negatively biased grid situated between the discharge chamber and the process chamber (that contains the substrate) accelerates the positively charged argon ions out of the discharge chamber and towards the substrate. This grid also ensures that the argon ions form a collimated beam. The process chamber is kept at high vacuum which maintains the high quality of the beam due the low concentration of contaminant molecules that could disrupt the path of the beam. Electrons are pumped into the process chamber via a filament to ensure that the chamber remains at a neutral overall charge.

The substrate is placed on a sample holder which, in turn, is attached to a chuck in the process chamber. This chuck can rotate to ensure uniformed milling. The entire rotary motor/chuck assembly can be tilted to select the desired milling angle.

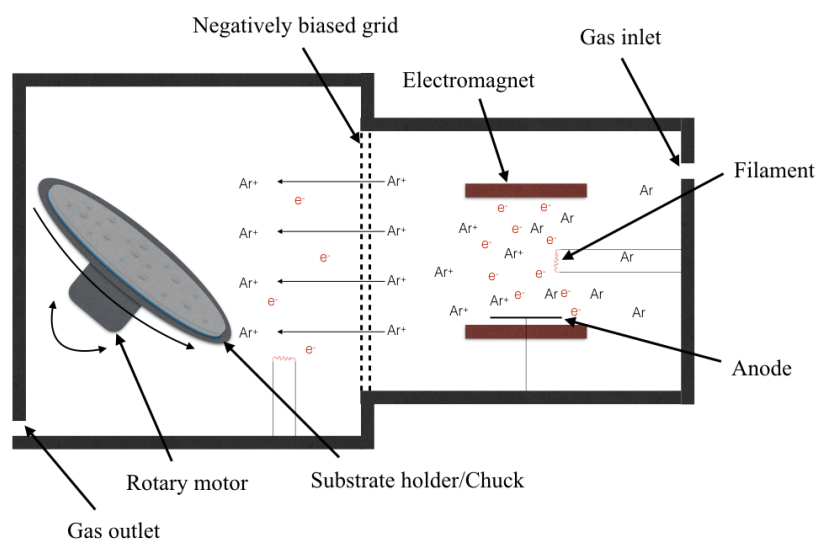


*Figure 16. A schematic showing the main components of an IBE tool. Argon is introduced to a discharge chamber via a gas inlet where it is ionized by electron bombardment and accelerated towards a rotating substrate by a negatively biased grid. Image based on [36]*

For this project, various milling parameters were tested. The roughness and the thickness of the remaining oxide were measured and this will be discussed in the next section, *Characterisation*.



*Figure 17. The final sensor. Dual-sized nanoantennas on glass, embedded in a thin layer of topographically flat silicon dioxide.*

## 4. Characterisation

Four properties of a completed sensor were characterised prior to use:

1. Spectrophotometry was used to determine the optical properties of the nanodisks and their suitability as dual-peak sensors. This was done for both corrugated and flat sensors
2. Atomic force microscopy (AFM) was used to determine the topography (roughness) of a milled sample as a means to quantify the flatness of a chip
3. Scanning electron microscopy (SEM) was used to inspect the condition of the nanodisks and to determine the thickness of the milled oxide layer embedding them
4. Bulk refractive index sensitivity (BRIS) was used to give an indication of the sensitivity and functionality of a sensor

### *Spectrophotometry*

Spectrophotometry measures the transmission or absorption of light by a sample as a function of wavelength. A schematic of the main components of a spectrophotometer is shown below and the general working principle is as follows: A light source, containing a range of wavelengths, is collimated by a collimator and directed towards a monochromator (grating or prism) which is used to separate this light into its constituent wavelengths. A slit is then used to select the range of wavelengths that are to be scanned. Before a selected wavelength is directed towards a sample, it is split with a beam splitter. One beam is sent directly to a photodetector as a reference and the other is sent to the sample. After passing through the sample this other beam also goes to a photodetector. By analysing the reference beam and the sample beam the tool software calculates the transmission of the sample at this wavelength.

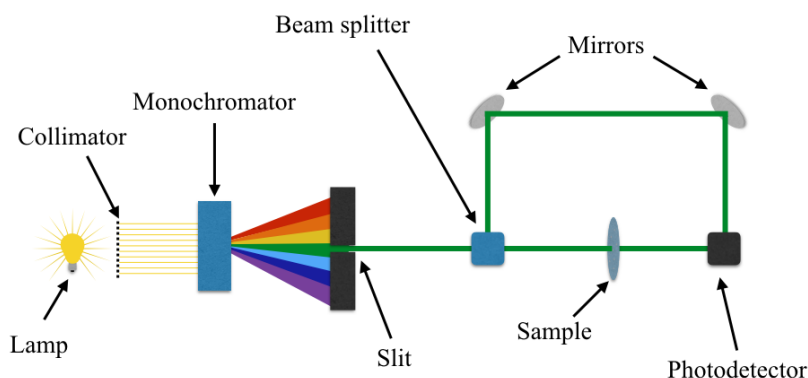


*Figure 18. A schematic of the primary components of a spectrophotometer. The tool used during this project was a Cary 5000.*

The transmission of a sample is inversely proportional to its extinction. As mentioned previously in the *Theory* section, the LSPR wavelength corresponds to the wavelength at which the maximum extinction occurs. Therefore, this would correspond to the wavelength of minimum transmission in this case. The transmission spectra obtained from the Cary spectrophotometer have been converted to extinction spectra for convenience in this report.

Spectrophotometric characterisation, while important for all nanoplasmonic sensors, was particularly important in this project. Good peak separation (Figure 19) is vital for functionality of a sensor. If both peaks cannot be tracked individually then the sensor will be non-functional. It is for this reason that spectrophotometric characterisation was also effectively a screening process.

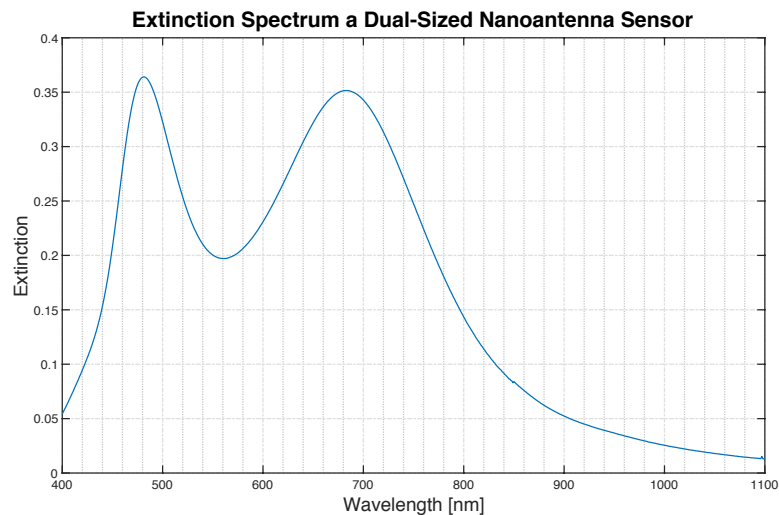


Figure 19. An example of a typical extinction spectrum for a dual-sized nanoantennas sensor as measured by a Cary 5000 spectrophotometer. This particular spectrum is for a sensor containing 80 nm and 190 nm disks embedded in 10 nm of silicon dioxide.

### *Atomic force microscopy*

AFM is primarily used to obtain information on the topographical profile of a sample. The technique utilizes a sharp tip scanned across the surface of a sample to produce images with a high vertical resolution. The tip is attached to a cantilever that is moved along a surface in a raster pattern controlled by a piezoelectric scanner. A laser is reflected off the cantilever towards a photodiode array as a means to detect changes in the orientation of the cantilever.

There are three main modes of operation associated with AFM: contact mode, tapping mode and non-contact mode, relating to the relationship between the tip and the surface during measurement. The mode that was used in this project was tapping mode. For this mode, the cantilever is oscillated by a piezo stack at its resonance frequency [37]. The laser reflecting off the cantilever detects this pattern. If the tip comes in contact with the surface, this pattern will be affected. The piezo stack can then change the total height for the cantilever until the resonance frequency is restored. This change in height corresponds to the height and depth of the features on the surface of the sample.

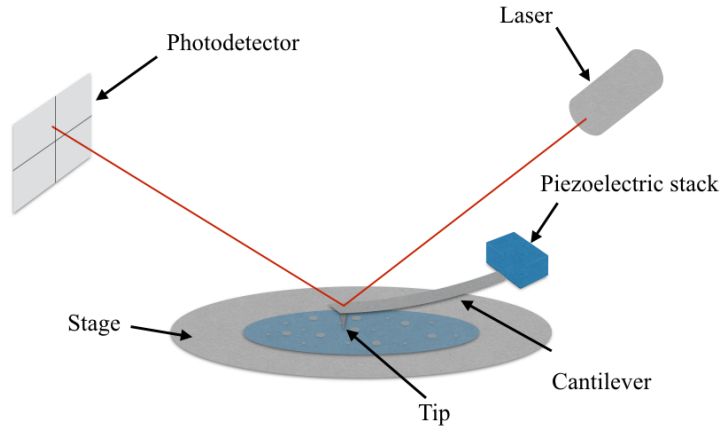


Figure 20. A schematic showing the main components of the AFM set up. As the tip is moved across the sample it becomes deflected by features on the surface. These deflections are detected by a laser reflecting off the cantilever towards a four quadrant photodiode.

For this project, AFM was used as a means to quantify the “flatness” of a milled sensor. In this work, it was defined as the root-mean-square of the height deviations,  $R_q$ , which was found for multiple  $1 \mu\text{m}^2$  regions and the average calculated.  $R_q$  is automatically calculated by AFM image analysis software such as Gwyddion or NanoScope using the following equation [38]

$$R_q = \sqrt{\frac{\sum Z_i^2}{N}} \quad (4.1)$$

where  $Z$  is the vertical height of a peak or trough and  $N$  is the number of these peaks and troughs.

The primary use of this information was to compare the milled chips to one another and to the roughness of a corrugated chip. The images obtained via AFM also gave a good indication of the general overall flatness of a sample.

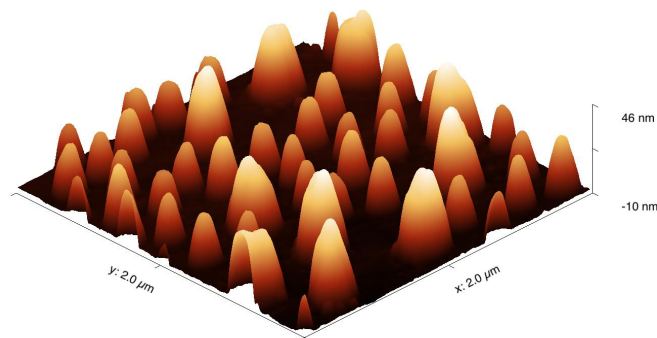
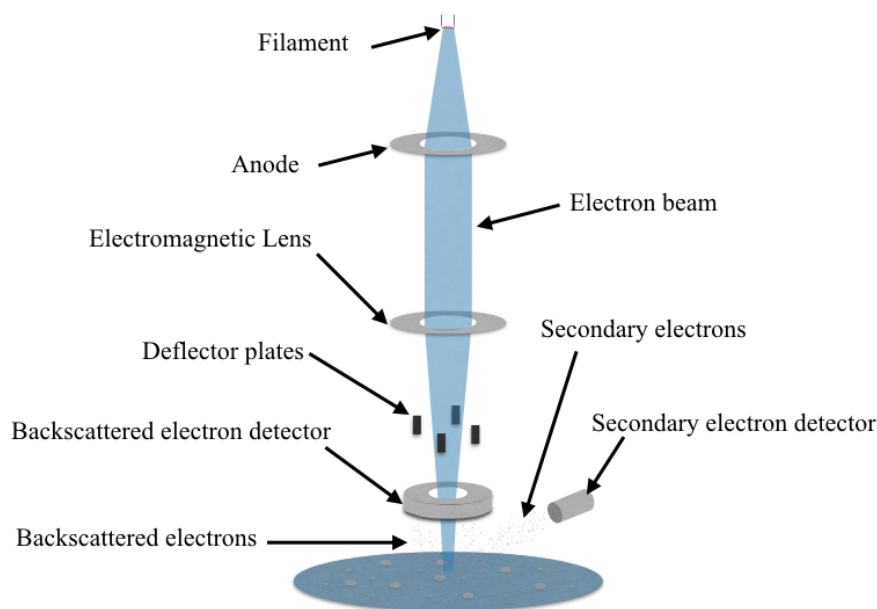


Figure 21. An example of an image obtained using AFM. This particular image is a  $2 \times 2 \mu\text{m}^2$  region of a sensor consisting of  $80 \text{ nm}$  and  $210 \text{ nm}$  disks covered in  $10 \text{ nm}$  of silicon dioxide. The roughness of this particular region was found to be  $11.79 \text{ nm}$ .

## Scanning electron microscopy

Many devices produced by nanofabrication are done so via multi-step processes. The ability to quickly and easily characterise a specimen between these steps, and after device completion, is extremely advantageous. SEM can be used to produce images with nanometer resolution and a magnification of over 3 million [39]. It is for this reason that it is one of the most widely used characterisation techniques in nanofabrication.

The high resolution of SEM is due to the fact that electrons are used to produce an image as opposed to light. The resolution of a microscope is constricted by the Rayleigh criterion, which shows that the distance between two individually resolvable points is directly proportional to the wavelength of the radiation used to form the image. The wavelength of an electron, which depends on its energy, is over 100 times smaller than that of a photon of light. These electrons, produced via thermionic or field emission, are accelerated under high vacuum by an anode towards the sample. Since the wavelength of an electron depends on its energy, the acceleration voltage can be used to control the resolution. Electromagnetic lenses are used to focus the accelerated electrons to a spot size between 1-5 nm; the resolution is also directly proportional to this. Deflector plates or scanning coils are used to direct the x-y direction of the beam to perform a raster scan of the sample.



*Figure 22. A schematic of the main components of a scanning electron microscope. High energy backscattered electrons are detected via an in-lens backscatter electron detector. Lower energy secondary electrons are directed towards a detector by a Faraday cage set to a positive voltage. This voltage is strong enough to attract the secondary electrons but not strong enough to attract the backscattered ones.*

Now that the electrons have been directed towards the surface, it is important to understand what occurs there. By knowing this, we can obtain important information from the electrons and photons detected after the beam has interacted with the specimen. The interactions are divided into two categories, elastic or inelastic scattering. Elastic scattering occurs when an electron from the incident beam strikes the nucleus of an atom and is scattered. These are known as backscattered electrons (BSEs) and give information on the topography and composition of a sample. The topography is determined by detecting all of the BSEs from one

side of the beam. The composition is determined by detecting the BSEs symmetrically around the beam. Larger nuclei will obviously scatter more electrons, which would result in a brighter spot in a BSE image. The contrast on these images can be analyzed to determine composition. There are numerous signals caused by inelastic scattering but the most analyzed of these is the secondary electron signal, which gives topographical information. These are electrons which gain enough energy from the beam electrons to escape the material. One incident electron can result in several secondary electrons. The number of electrons detected is related to the gradient of the surface that the beam is striking, as shown in Figure 23. Also, since the energy of a secondary electron is much lower than for a BSE, these come from within a 20nm range from the surface, compared to >100nm for BSEs, resulting in a better topographical resolution. The other main signals, which were not analyzed for this project, are X-rays, Auger electrons and cathodoluminescence, all of which are the result of inelastic scattering and give information on the composition and properties of the sample.

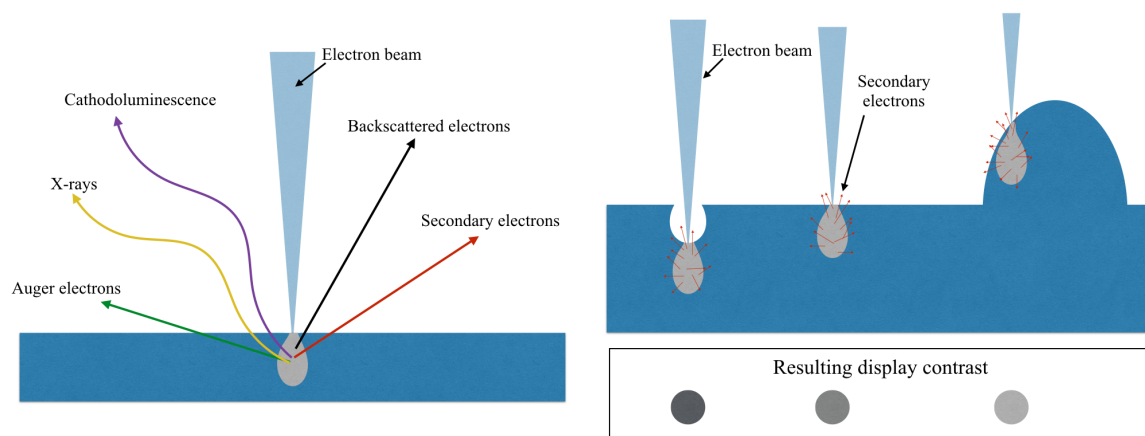


*Figure 23. Two figures showing the beam-surface interactions. On the left: The signals produced by an electron beam incident on the surface of a sample. On the right: The mechanism by which secondary electrons can be used to obtain topographical information. This schematic shows how the number of secondary electrons that escape from a sample is dependent on the surface topography. The display contrast is then dependent on the number of detectable electrons.*

Since SEM uses electrons to bombard a sample it is necessary to ground the sample to prevent the accumulation of charge. For most SEM setups, this stipulates that the sample must be conducting. Since the device fabricated in this project was based on a glass substrate, which is not conducting, silicon was used for any potential SEM measurements. Therefore, this required silicon based devices to be manufactured in parallel with all glass devices, solely for this purpose.

In this project, SEM was used primarily for two things: to investigate the condition of the disks and to measure the post-milling oxide thickness. After the completion of the HCL process, and prior to PECVD, it was sometimes necessary to inspect the condition of the disks for signs of agglomeration. This was mainly needed only when researching new PS bead mixtures. After milling a silicon based chip, it was broken in half using a diamond tip pen to enable a cross section view on the silicon-nanodisk-silicon oxide layer. Due to the aforementioned ability of SEM to differentiate between composition it was possible to detect the oxide layer and measure its thickness. The targeted post-milling oxide thickness was 10 nm above the antennas, which equated to 30 nm from the substrate.

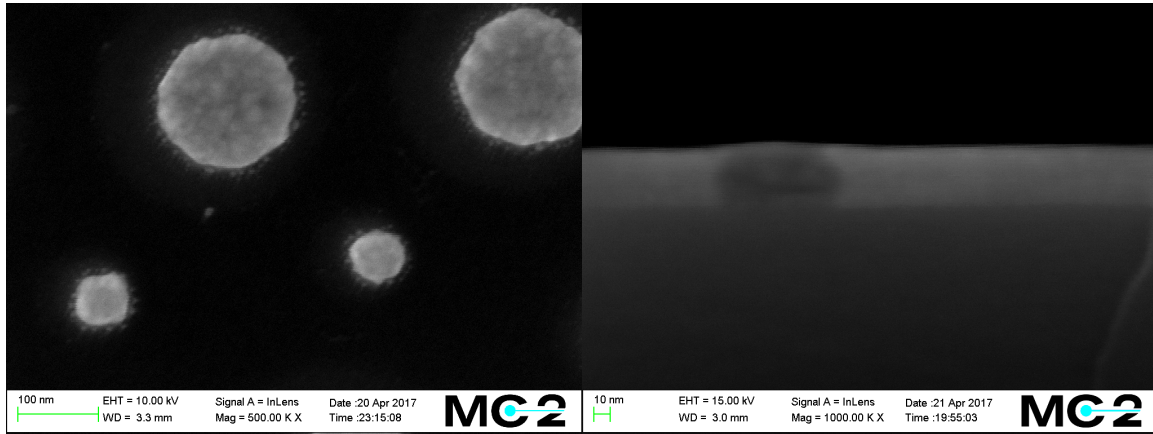


Figure 24. Images produced using a Zeiss Supra 60 VP SEM. On the left: The top-down view of silver disks on silicon produced using HCL. These disks were produced using PS beads of 80 nm and 190 nm. On the right: The side view of a sample consisting of silicon covered in silver disks and embedded in silicon oxide which was then milled to produce a flat surface. The bottom half of the image is the silicon substrate. A silver disk surrounded by oxide can be seen on top of this.

### *Bulk refractive index sensitivity*

In order to assess the suitability of a device as a nanoplasmonic ruler it was necessary to evaluate its sensitivity to changes in the refractive index of the medium in its immediate vicinity. BRIS was used for this purpose. It was this technique that was also used to obtain the sensitivity factor,  $S$ , mentioned in the *Theory* section, and used in the calculation of thin film thickness,  $d_f$ . It will be discussed further in the *Adsorption Measurement* section but briefly mentioned here.

In essence, the technique exposes the sensor to multiple mediums of known refractive index and measures the LSPR response. As a characterisation technique, this was mainly used to assess the milled samples. This was due to the fact that the decay length of a disk is affected by the thickness of the oxide layer that it is embedded in. Excessively thick samples would decrease the decay length, and hence the sensing volume, resulting in a low  $S$  value. A relatively low  $S$  value, as the name suggests, would imply that a given sensor would also have a low sensitivity, i.e. a large change in refractive index resulting in a small LSPR response. This would result in a larger noise in measurement results.

It is also important to remember that dual-sized nanoantennas have two LSPR responses, therefore, a BRIS measurement will give two results, one for the large antennas and one for the small antennas.

BRIS and SEM were used in conjunction with each other to determine the minimum oxide thickness that could protect the nanodisks while still permitting a sufficiently large LSPR response to refractive index changes beyond the oxide.

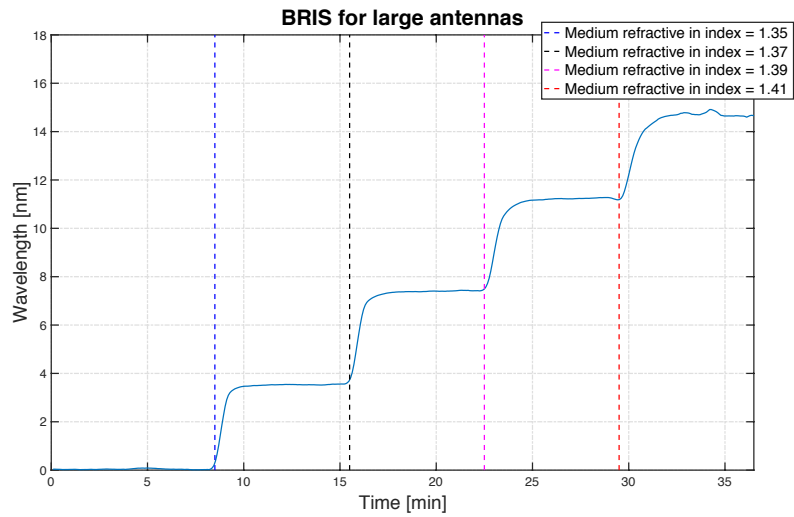


*Figure 25. An example of a typical BRIS measurement. The refractive index of the medium surrounding a sensor is increased in steps over time. The sensor responds with an increase in the LSPR wavelength for the nanodisks on the surface. This particular BRIS is of the peak shift for antennas of a 190 nm disk diameter embedded in 10 nm of silicon nitride (corrugated chip).*

## 5. Adsorption Measurement

### *Equipment*

Adsorption measurements were carried out using the XNano tool produced by Insplorion. The device into which the sensor was loaded consisted of titanium cartridge with a liquid inlet and outlet and a transparent window through which light could propagate. The volume above the sensor was approximately 4  $\mu\text{L}$  and the measured spot size approximately 2 mm in diameter [40].

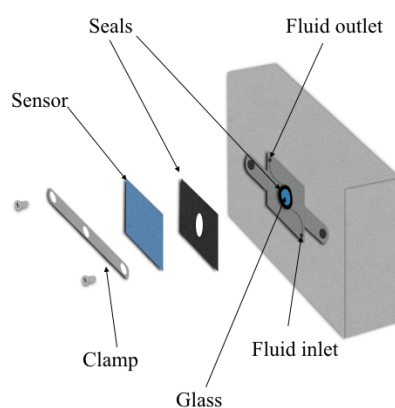


*Figure 26. A schematic of the XNano loading cartridge. The sensor was mounted using the clamp shown above via two screws. Two seals were used to form a liquid-tight measuring volume between the sensor and a glass window through which light from a lamp could propagate through the sensor and out a hole in the clamp towards a spectrometer. Two holes, connected to the measuring volume via grooves machined in the cartridge, served as the inlet and outlet for fluids.*

The lamp used to illuminate the sensor and cell was a tungsten-halogen lamp. This was connected to the cell via an optical fiber, which, in turn, was connected to a spectrometer, also via an optical fiber. The optimal wavelength measurement range for this spectrometer was 400 – 1100 nm. This enforced some limitations on the diameter of the PS beads that could be used in the fabrication process and will be discussed in more detail in the *Results and Discussion* section.

Fluids were introduced to the cell using a peristaltic pump. This was placed between the sample vial and the cell to push fluids into the cell as shown in Figure 27. This setup minimizes the risk of introducing air bubbles to the system that might occur if the pump was situated on the outlet line and a sucking mechanism used to introduce the sample.

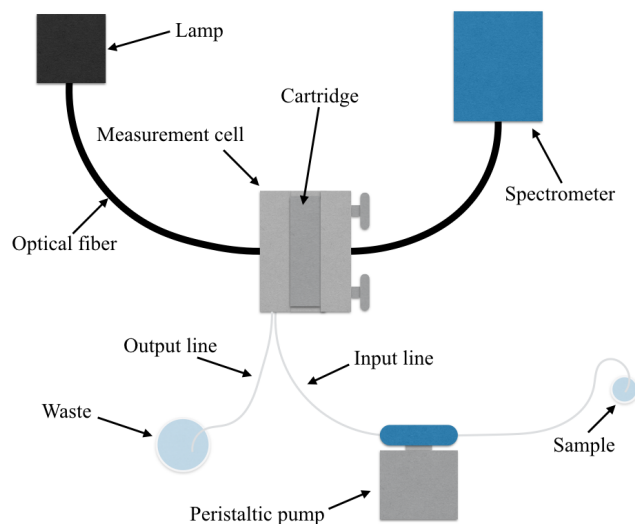


Figure 27. The setup for measurements using the Insplorion XNano system. The cartridge was clamped into the measurement cell via two hand-tightened knobs.

The spectrometer was connected to a PC and the Insplorer® software was used to control and monitor all measurements. During measurement mode, the user interface consisted of a spectrogram showing extinction vs wavelength measured at a frequency selected by the user (0.2 Hz was used for this project) and another window displaying the shift of a peak in this spectrogram versus time. This enabled a real-time observation of a peak shift corresponding to the LSPR response due to refractive index changes in the cell. The software allowed for the tracking of the maximum peak amplitude and/or the peak centroid, which is the “centre of mass” of a peak. Tracking the maximum peak amplitude of a broad peak tended to produce noisy spectra due to the lack of a sharp, well defined peak. In this scenario, centroid tracking was used as the preferred data source since centroid tracking significantly reduces noise [41]. However, since most LSPR peaks are asymmetric, the centroid and the actual peak positions were not always the same. For this reason, the tracking method of choice must be maintained for all data analysis for any given measurement.

### *Adsorption measurement methodology*

The adsorption measurements consisted of five main steps:

- I. Preparation
- II. BRIS measurement. From this it was possible to obtain the  $S$  value for both antenna sizes for the sensor. This value was necessary for various calculations, unique for each sensor and unique for the two disk sizes that the sensors were comprised of.
- III. Lipid addition. A lipid of a known length and refractive index was adsorbed to the surface in order to calculate the decay length of the sensor. Again this value was unique to each sensor and to both disk sizes.
- IV. Adsorption of the analyte. The analytes tested with this system were as lipid binding protein and a lipid binding DNA.
- V. Data analysis

## I. Preparation

Prior to all measurements it was necessary to obtain the baseline for the experimental setup. This was due to the fact that the baseline can be affected by factors such as condition of the lamp and the position of the fibers, factors that change on a daily basis. This was done by loading the measurement cell with a blank glass slide and subjecting the cell to a constant flow of MilliQ water. A dark spectrum (obtained while the lamp was turned off) and a bright spectrum (obtained when the lamp was on) were taken and used to calibrate the baseline using the Insplorer® software. The condition of the baseline could be tested by running a measurement using this blank slide and MilliQ.

When a stable baseline was achieved, the sensor could then be loaded into the cell. Prior to loading, this sensor was rinsed in MilliQ and dried under nitrogen. After sensor loading, the cell was again subjected to a constant flow of MilliQ and the parameters were set up. This was done by measuring the spectrum for the sensor and selecting the analysis range and centroid range for the peak of preference for real-time tracking. The software did not enable dual-peak tracking but by selecting the inflection point of the other peak it was possible to track it, to some degree, in real-time.

At this stage it was necessary to run what we will call a “dummy measurement”, a measurement without any analyte. During this measurement only MilliQ flowed through the cell. The purpose of this was to wait until a stable baseline was achieved for the shift vs time spectrum.

## II. BRIS

Once this stable baseline was achieved it was possible to start the measurements, the first step being the analysis of the sensor's sensitivity. This was done, as previously mentioned, using BRIS. Every 7 minutes the cell was subjected to solutions of varying concentrations of glycerol in MilliQ. For the first 7 minutes of the measurement pure MilliQ was used, which has a refractive index of 1.33. Upon changing between any solutions it was necessary to turn off the pump to avoid the introduction of air bubbles to the cell. For each solution the refractive index was known. The concentrations and corresponding refractive indices used for this project were: 14 wt% glycerol = 1.35, 29 wt% = 1.37, 44% = 1.39 and 58% = 1.41 [42]. Ethylene glycol was also used for BRIS measurements in the early stages of the project. For BRIS measurements, a flowrate of 100  $\mu\text{L}/\text{min}$  was used.

Through the linear regression of a BRIS measurement such as that shown in Figure 25, it was possible to obtain a plot such as that shown in Figure 28, the slope of which corresponds to the  $S$  value. This was necessary for the equations 2.32, 2.34 and 2.33 for the calculation of the decay length, the refractive index and to plot the film thickness vs peak shift ratio, respectively.

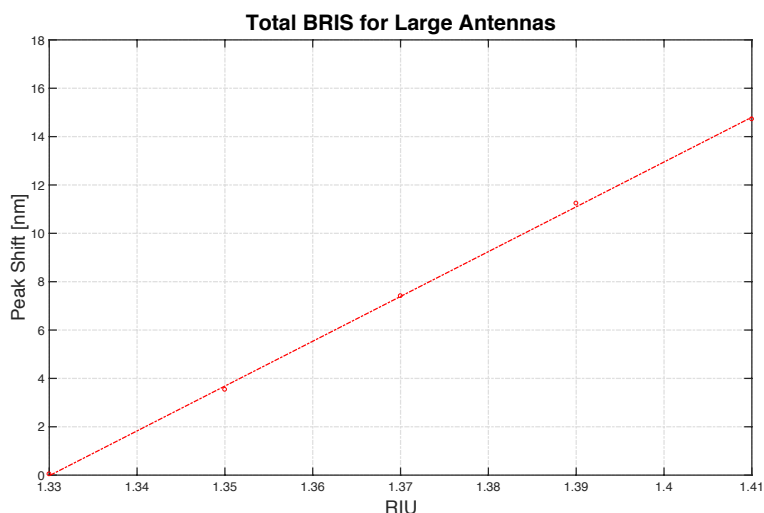


Figure 28. The typical plot obtained from the linear regression of a BRIS measurement. The slope of this gives the  $S$  value. This particular plot is the linear regression of Figure 25 and the  $S$  value obtained for the 190 nm disk belonging to this sensor was 185.33 RIU/nm.

### III. 1-palmitoyl-2-oleoyl-sn-glycero-3-phosphocholine (POPC) adsorption

After the BRIS measurement, another dummy measurement was necessary. This consisted of subjecting the cell to a constant flow of a buffer solution and again waiting for the baseline to stabilize. The buffer of choice depended on the buffer in which the biological samples to be tested were contained. A buffer is a solution whose pH remains relatively stable upon the addition of a small amount of strong acids or bases. They are used extensively in biology to provide biological molecules with a stable environment. The buffers used in this project were Bis-Tris (2,2-Bis(hydroxymethyl)-2',2''-nitrilotriethanol, 2-Bis(2-hydroxyethyl)amino-2-(hydroxymethyl)-1,3-propanediol, Bis(2-hydroxyethyl)amino-tris(hydroxymethyl)methane) and PBS (phosphate-buffered saline), both of which contained NaCl and had a pH value of 7.4.

When a stable baseline was achieved, a POPC adsorption measurement was started. POPC is a phospholipid that can adsorb to the surface of the sensor to form a lipid bilayer of a known thickness and refractive index, which are 5 nm and 1.48, respectively [43] [44]. These lipids were in the form of vesicles while in solution. The flowrate was reduced to 50  $\mu\text{L}/\text{min}$  and buffer was pushed through the cell for the first 10 minutes, after which a solution containing 0.1  $\mu\text{g}/\text{mL}$  POPC in the same buffer was introduced. After approximately 25 minutes, due to a significant peak shift and subsequent baseline stabilization, it could be assumed that adsorption had occurred. At this stage, pure buffer was reintroduced to the cell. If the baseline remained stable the experiment could continue to the adsorption of the analyte.

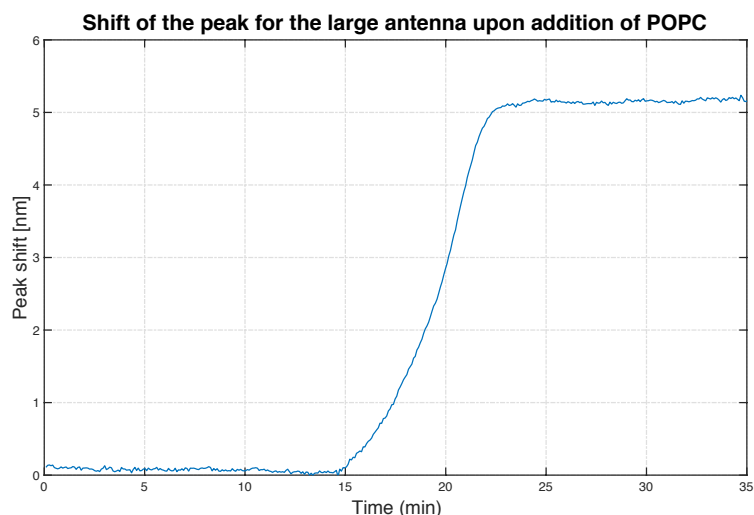


Figure 29. The typical LSPR response upon the addition of POPC to the cell and its adsorption to the surface of a sensor. The commencement and completion of the adsorption process can be seen clearly by the initial increase in the peak shift and its subsequent return to a stable flat line (approximately 7 minutes later), respectively.

#### IV. Analyte adsorption

Between the POPC adsorption and the analyte adsorption the measurement was continued, i.e. the measurement process was not restarted and the POPC adsorption, followed by analyte adsorption, were contained of the same plot, as shown in Figure 30. After approximately 10 minutes of post-POPC-adsorption buffer addition, the flowrate was reduced to 20  $\mu\text{L}/\text{min}$ . Buffer was pushed through the cell for another 10 minutes at this rate to ensure that the lipid bilayer was indeed stable. The analyte was then introduced to the cell and continued to be pushed through until the sample dropped to a level too low to risk the addition of air bubbles to the system or until any visible LSPR response had stabilized. The analytes used in this project were a DNA, ABCD-DNA, and a protein, phospholipases A2 (PLA). Both are known to bind to lipids, with the latter facilitating lipid decomposition through hydrolysis over time.

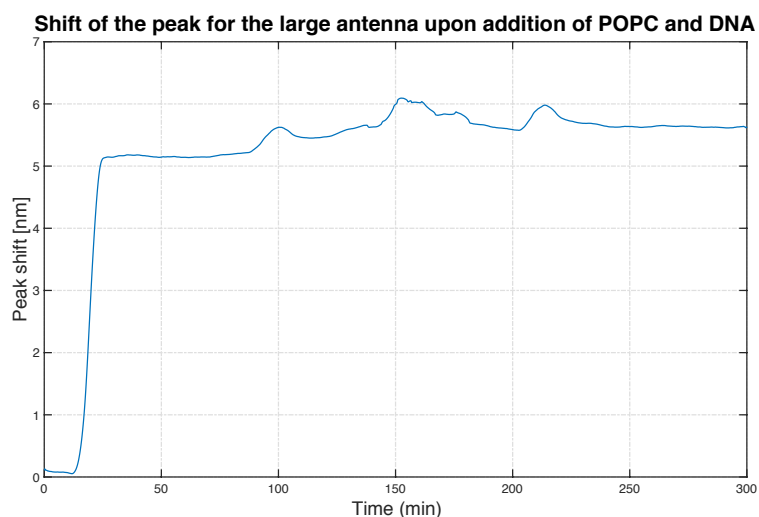


Figure 30. POPC adsorption followed by analyte adsorption (after  $\sim 80$  minutes). Although somewhat masked by anomalies, possibly caused by air bubbles, between  $\sim 80$  and  $\sim 230$  minutes, there is relatively distinguishable peak shift from the formation of the POPC lipid bilayer to the adsorption of the analyte to the bilayer.

## V. Data analysis

After the completion of all measurements it was possible to recalculate all the curves to obtain the peak maximum amplitude shifts and centroid shifts for the both peaks produced by the large and small antennas. For each nanoantenna size (large or small), the corresponding  $S$  value was used in conjunction with the corresponding LSPR responses upon the addition of POPC to calculate the decay lengths using equation 2.32.

For example, from Figure 28 and Figure 29 it can be seen that  $S_{\text{large antenna}} = 185.33 \text{ nm/RIU}$  and the LSPR response to POPC addition,  $R_{\text{large antenna}} = 5.136 \text{ nm}$ , respectively. By inserting these values into equation 2.32, along with the known refractive index and thickness of a POPC bilayer, 1.48 [44] and 5 nm [43], respectively, and taking the refractive index of the bulk solution,  $n_b$ , to be 1.33 since it was primarily water, it is possible to calculate the decay length for the large antennas for peak shift measurements.

$$\delta_{\text{large antenna}} = - \frac{d_f}{\ln \left( 1 - \frac{R_{\text{large antenna}}}{S_{\text{large antenna}} (n_f - n_b)} \right)}$$

$$\delta_{\text{large antenna}} = - \frac{5 * 10^{-9}}{\ln \left( 1 - \frac{5.136 * 10^{-9}}{185.33 * 10^{-9} (1.48 - 1.33)} \right)}$$

$$= 24.478 * 10^{-9} \text{ m}$$

This same technique was used to calculate the decay length for the small antennas by using the unique  $S$  value and LSPR response measured for these antennas.

From these  $S$  values and the newly obtained decay lengths it was possible to produce a theoretical plot of the ratio of the LSPR responses for the large and small antennas vs film thickness using equation 2.33.

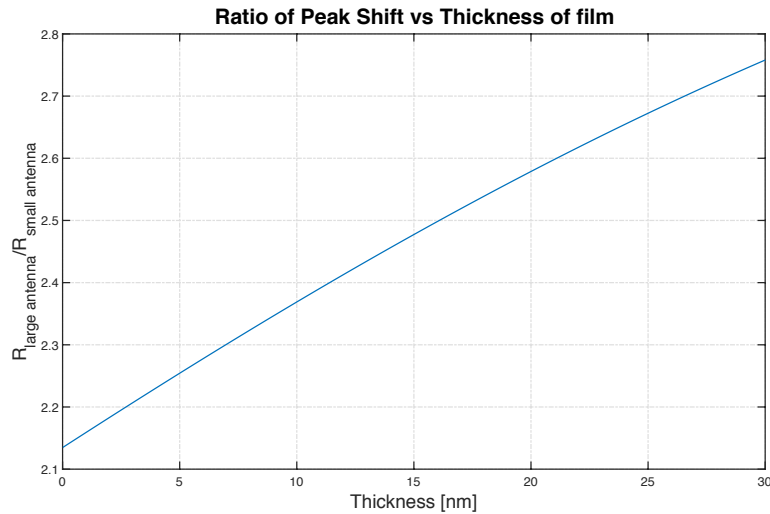


Figure 31. A plot of the ratios of the LSPR responses for the large and small antennas vs the thickness of a film that would induce these responses.

The measured ratios could then simply be located on this graph to obtain the corresponding thickness of the total adsorbed film (the lipid and analyte) that would produce this specific ratio. Finally, with this thickness, equation 2.34 was used to calculate the refractive index of these adsorbed entities.

## 6. Results and Discussion

### *Fabrication*

This section will focus solely on the fabrication of the corrugated and pre-milled sensors, mainly on the PS bead mixtures and their effect on the spectra of the sensors.

### Peak separation

The first requirement when fabricating a sensor that utilizes the LSPR response of two separate peaks was to obtain these two peaks. As mentioned previously, the LSPR wavelength is affected by the size a particle and, hence, the size of the PS beads used to produce the silver disks for this project.

Multiple PS bead mixtures were tested, each mixture consisting of a small bead size and a larger bead size, to maximize peak separation. The small bead sizes that were assessed were 80 nm and 100 nm and the larger beads were 190 nm, 210 nm and 230nm. The extinction spectra for silver disks fabricated using these 5 bead sizes are shown below. The three main reasons for investigating various PS bead mixtures were: to obtain good peak separation, obtain peaks that were relatively narrow and to ensure that both peaks would be contained within the optimal analysis range for the XNano spectrometer, which, as previously mentioned, was 400 – 1100 nm.

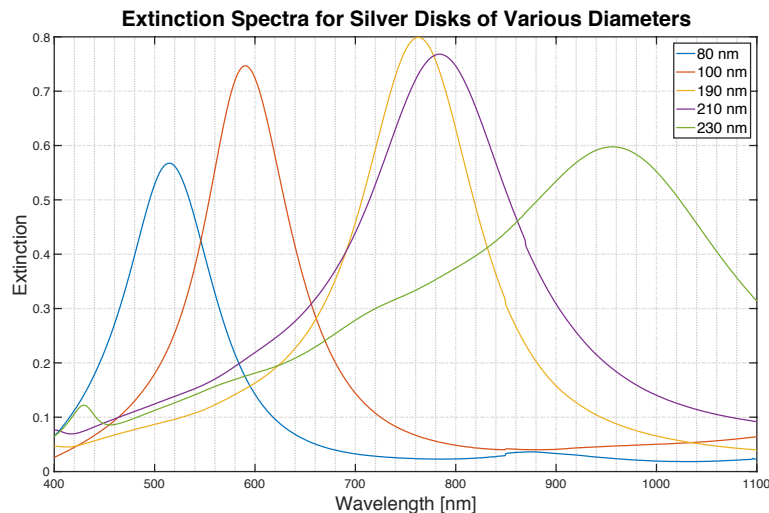


*Figure 32. A plot of the extinction spectra for unembedded silver disks of various diameters. Each plot is labelled with the diameter of the beads used in their fabrication process.*

All of the peaks in Figure 32 were within the desired range. From these spectra, it could be assumed that any mixture of small and large beads would produce a functional sensor. However, these disks had not been embedded in silicon dioxide or silicon nitride yet. It was considered likely that upon the deposition of a dielectric that all of these peaks would red-shift (increase in wavelength). This was assumed because the refractive index of these dielectric materials is larger than that of air and since, as shown by equation 2.29, increasing the refractive index of a medium surrounding a particle increases the LSPR wavelength, this red-shift was expected. As seen from Figure 33 below, this was not the case.

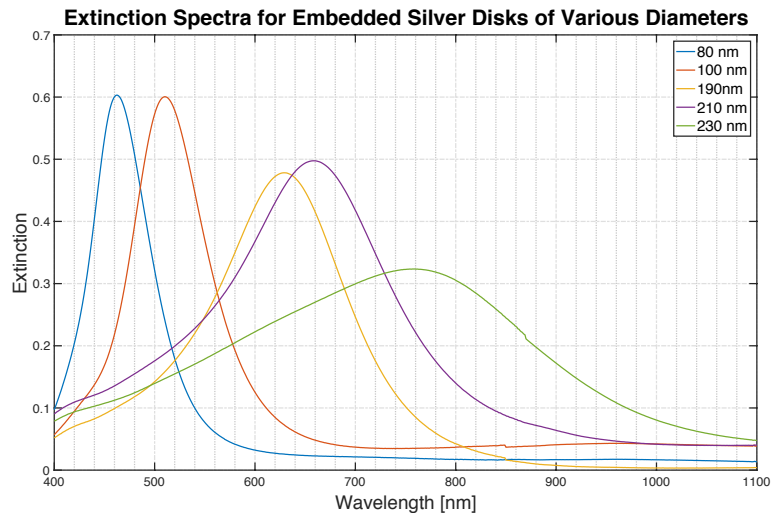


Figure 33. A plot of the extinction spectra for silver disks of various sizes embedded in 10 nm of silicon dioxide. Again, the plots are labelled with the diameter of the PS beads used in their fabrication process.

It was found that upon the deposition of silicon dioxide that the peaks in fact blue-shifted (decreased in wavelength), with the larger peaks shifting to a greater extent. One possible reason for this may be silver's susceptibility to oxidation. The temperature of the heated table in the PECVD chamber, which was 300°C, along with the presence of a powerful oxidising agent in nitrous oxide [45], was perhaps enough to cause some oxidation of the silver. This may have reduced the size of the disks, which would result in a blue-shifted response. However, this is just speculation and further investigation would be necessary. The blue-shift experienced due to the PECVD step may have also been exacerbated due to inexperience with the equipment which meant that the parameter set-up took longer and exposed the bare silver disks to this temperature for a longer time than usual. When put in 300°C, the disks “shrink” due to this relatively high temperature. At a high temperature, silver can become recrystallized. During this process, the crystal lattice for the particle becomes more ordered and the overall diameter of the disks decreases. This leads to a blue-shift and would explain why there was some degree of this shift occurring for all the sensors that were made throughout the project and this was taken into account when selecting the bead sizes prior to fabrication. It was also noted that this shift was more pronounced for the deposition of silicon dioxide than for silicon nitride, perhaps supporting the theory that some silver oxidation occurred upon silicon dioxide deposition in the presence of nitrous oxide. This was one of two reasons why all of the sensors produced in the later stages of the project were embedded in silicon nitride, the other reason will be discussed later.

There were two main results of this blue-shifted response upon embedding in silicon dioxide that were of interest for this project. Firstly, it meant that all the peaks remained within the desired range and, secondly, that the separation of the LSPR peaks for the large and small disks was reduced. For example, the distance between the peaks for disks produced with 100 nm beads and those produced with 190 nm beads was approximately 170 nm prior to embedding. After embedding, this is reduced by approximately 50 nm. It could no longer be assumed that any mixture of large and small beads selected for this project would produce a functional sensor. This is shown in Figure 34.

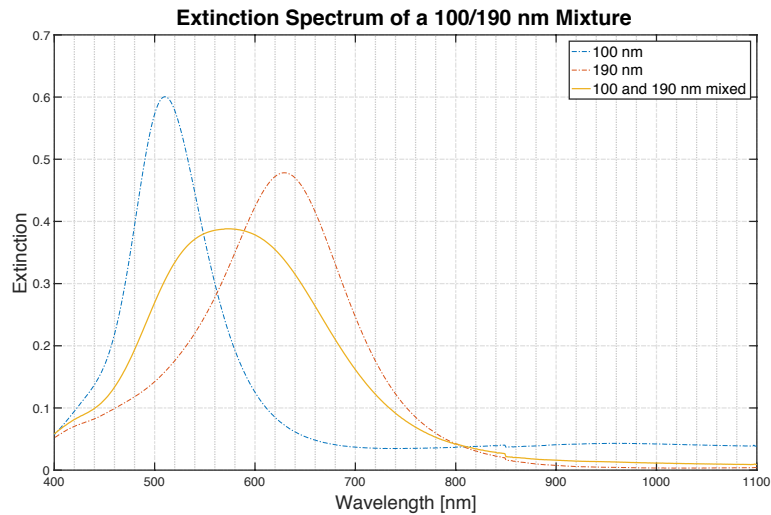


Figure 34. The extinction spectrum of an embedded sensor fabricated using a mixture of 100 and 190 nm PS beads, the spectra of embedded chips fabricated using unmixed PS beads of these sizes are also shown as reference.

From Figure 34, it can be seen that when the difference in diameter between the large and small beads is not sufficient that the peaks can merge. This only occurred for the mixture containing 100 nm and 190 nm diameter beads. The mixtures that were tested in this project that provided sufficient peak separation were (small bead/large bead): 80/190 nm, 80/210 nm and 100/230 nm.

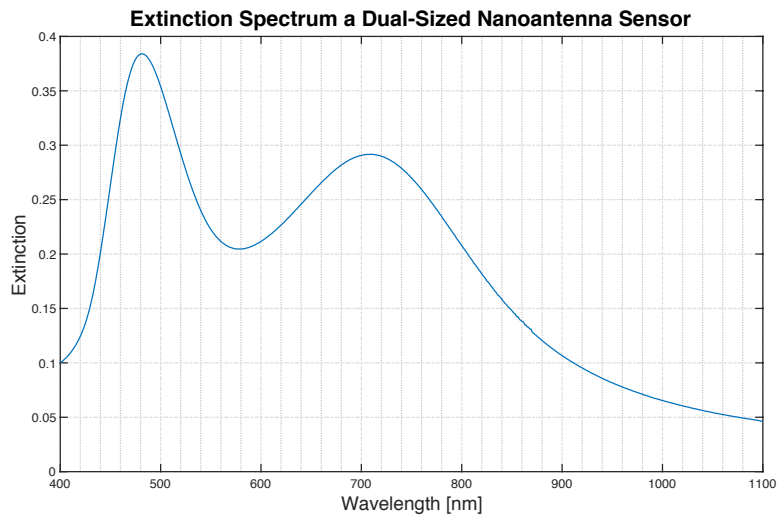
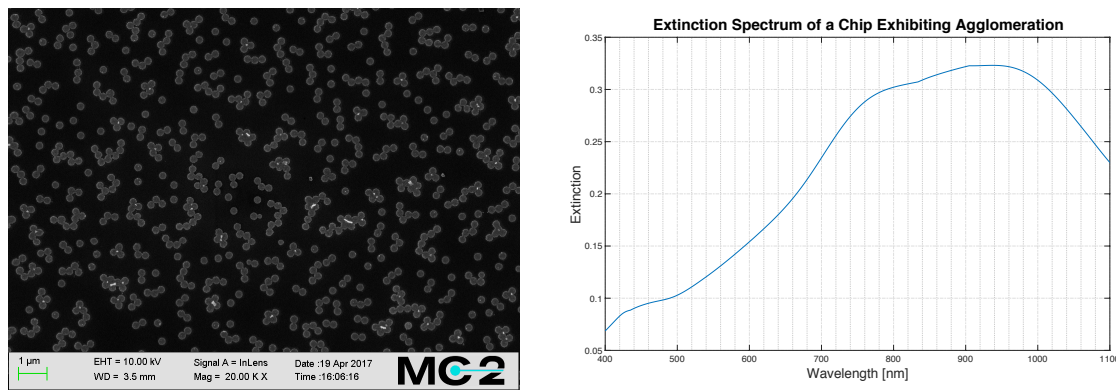


Figure 35. The extinction spectrum for a sensor fabricated using a mixture of 80 and 210 nm PS beads. This produced a sufficient peak separation for distinct peak tracking while also remaining within the desired analysis range.

### Peak width

Another issue that affected the functionality of a sensor was the broadness of the peaks. This was not really an issue with the peaks from the smaller disks. In Figure 33, it can be seen that the broadness of the majority of the peaks increases after the embedding process. However, as can be seen in Figure 32 for the 230 nm spectrum, this broad peak exists before embedding in silicon dioxide. This suggested that some broadening effects were due to the disks themselves. In order to investigate this further, SEM images were taken of the disks. It was found that the main cause of peak broadening was due to agglomeration of the beads on the surface during the fabrication process, which is a more common occurrence for larger beads. This resulted in disks that were physically joined, forming larger particles with different shapes and, therefore, with new LSPR wavelengths and others that were at least close enough to each other to affect their respective LSPR wavelengths. This resulted in a collection of new signals across a wider range than if all disks were the same, and hence, the broadening effect. An extreme version of this, with the corresponding extinction spectrum, is shown below. Since the decay length for larger antennas is longer than for smaller antennas, they are more susceptible to shifts in the LSPR wavelength due to neighbouring particles, which may explain why peak broadening appeared to be an issue with their corresponding peaks only.



*Figure 36. An SEM image of silver disks fabricated using a 230 nm PS bead solution and the corresponding extinction spectrum of an unembedded chip made with the same solution. The broadness of the peak in the spectrum can be attributed to the agglomeration seen in the SEM image.*

There are two main causes of PS bead agglomeration on the surface of the substrate during the fabrication process, solution contamination and mistakes in the fabrication process itself. The former can be mitigated by ensuring that all solutions are viable before the mixing process for the dual-size nanoantennas fabrication, which can be done via SEM like shown in Figure 36; the latter can be mitigated by performing extensive sonication on all mixtures prior to particle dispersion and to ensure extensive drying with nitrogen after the post-dispersion rinse.

## Milling

The suitability of the milling parameters was assessed by surface roughness and remaining oxide thickness. The chip that ranked highest when considering both of these criteria had an average roughness of 1.14 nm and an average oxide thickness of 29.74 nm. When comparing this to a corrugated chip with the same antennas, which had an average roughness of 11.31, this corresponds to an 89.9% decrease in the roughness value of the original, corrugated sensor. This difference can also be seen from the AFM and cross-sectional profile images below. A SEM image of the oxide thickness is also shown.

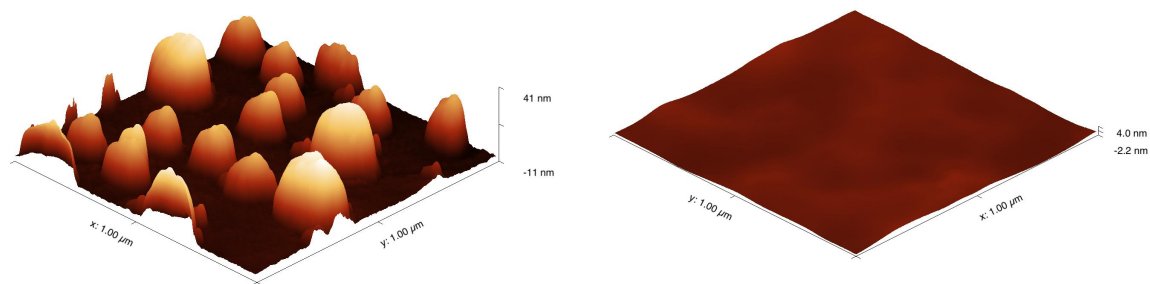


Figure 37. Two AFM images of a corrugated sensor (left) and a milled sensor (right). The milled sensor has a more uniformed surface and a maximum amplitude (as seen from the scale bar) approximately 10 times smaller than the corrugated sensor. Both sensors were produced using the same PS bead mixture of 80/190 nm and their HCL fabrication was executed in parallel.

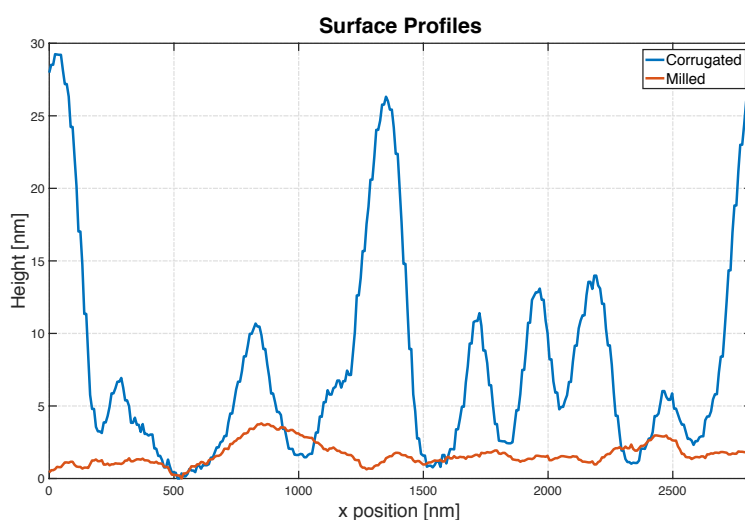


Figure 38. A cross-sectional surface profile of a corrugated sensor and a milled sensor. Both of these sensors are from an 80/210 nm PS bead mixture and the milled surface roughness is 89.5% smaller than that of the corrugated sensor. This also highlights the reproducibility of the milling technique as a means to produce flatter sensors.

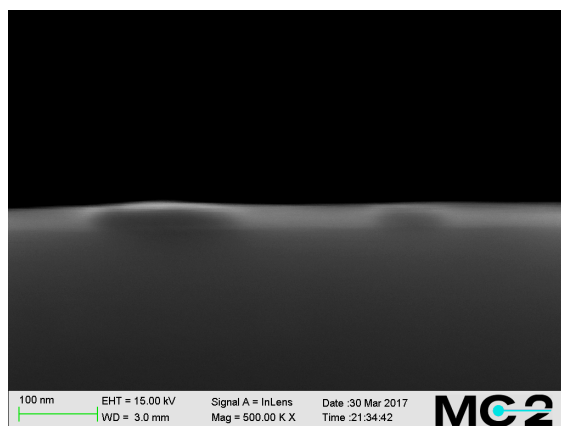


Figure 39. An SEM image of a cross-section of the milled sensor from Figure 37, that was used to measure the oxide thickness. The measurement was done using the Zeiss SEMs imaging software. The substrate, oxide layer and two disks of different sizes embedded in this oxide can be seen in the image.

When comparing the extinction spectra for milled and corrugated sensors, the main difference was in the position of the peaks. As shown in Figure 40, the milled sensors are red shifted. Since the sensors are totally embedded, this is to be expected. More silicon dioxide surrounds the milled, flat sensors which “fills up” the sensing volume of the sensor and red-shifts the LSPR wavelength.

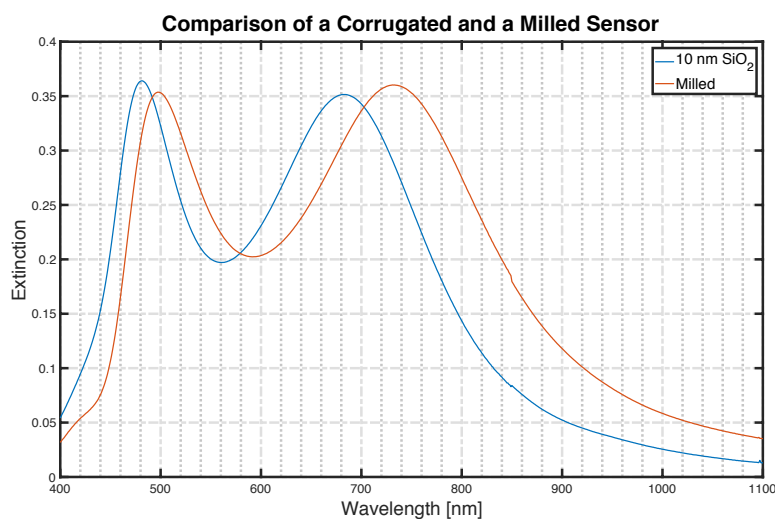


Figure 40. The extinction spectra for a milled, flat sensor and a corrugated sensor. Both were fabricated using the same PS bead solution which was 80 and 190 nm.

A lipid adsorption measurement was carried out to investigate the effects of surface roughness on the adsorption. The sensor used in this experiment was milled using the initial parameters of the project and had an average surface roughness of 1.313 nm, while the corrugated sensor had an average roughness of 8.163 nm, therefore the milled chip was 83.9% less rough. The nanoantennas for these sensors were 80 and 210 nm for both.

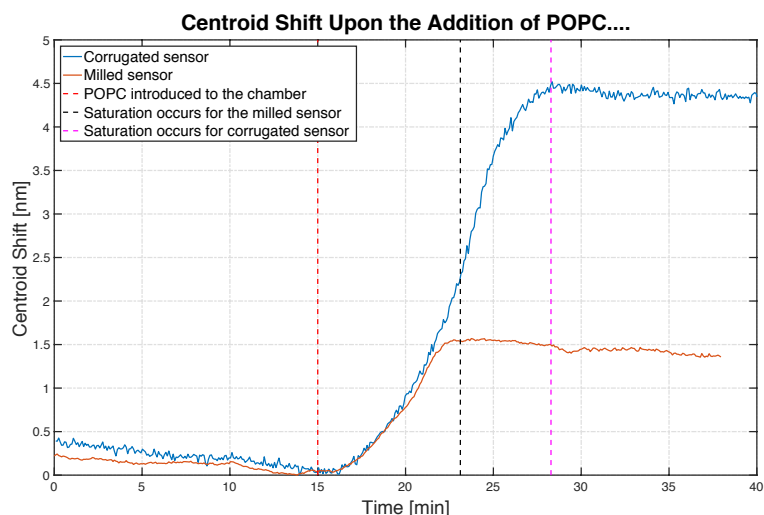


Figure 41. A figure showing the LSPR centroid shift upon the adsorption of a lipid bilayer to two different sensors, one corrugated and one milled to decrease surface roughness. The plot also indicates the times at which the lipid (POPC) was introduced to the chamber and centroid shift stopped for each sensor.

When the lipids first adsorb to the surface they are in vesicle form. After a few minutes these vesicles rupture and a bilayer starts to form. This rupture point is seen as a kink in the LSPR shifts in Figure 41, after ~21 minutes for the milled sensor and ~22 minutes for the corrugated. As can also be seen from Figure 41, the LSPR shift for the milled sensor reaches completion significantly faster than for the corrugated sensor. This most likely due to strain on the lipid bilayer from the raised disks of the corrugated sensor slowing down the bilayer formation [22].

Another noticeable factor from this figure is that the total shift for the milled sensor was quite a lot smaller than for the corrugated one. BRIS measurements carried out on various milled sensors confirmed the reduction in sensitivity for milled sensors vs corrugated sensors.

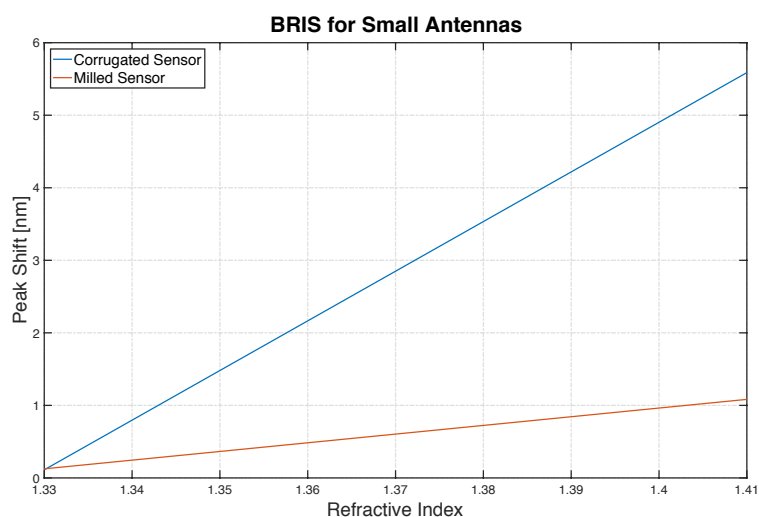
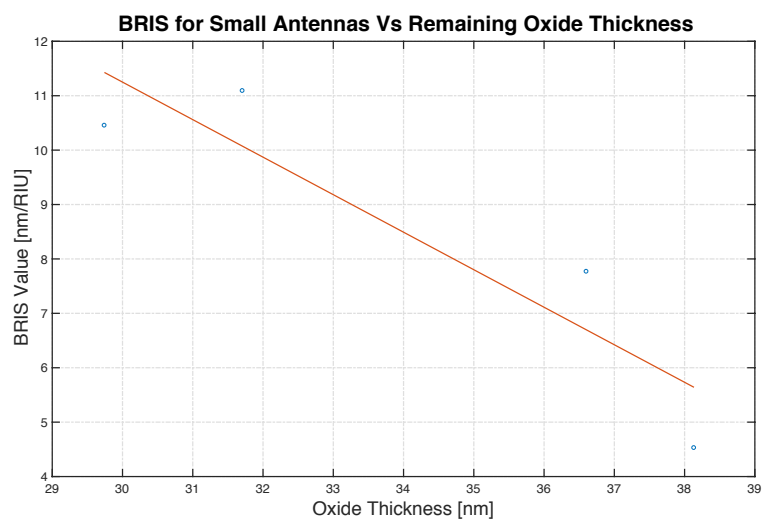


Figure 42. The linear regression of BRIS measurements taken for the small antennas of a corrugated sensor and a milled sensor. Both sensors were fabricated with an 80/210 nm PS bead mixture. The slope ( $S$  value) for the corrugated sensor is significantly larger than that of the flat sensor.

This reduction in sensitivity was more pronounced for the smaller antennas. It was sufficient to render many on the milled sensors dysfunctional, or at the very least, unreliable due to the increase in error via the decreased signal to noise ratio for these smaller antennas. This is most likely caused by the fact the disks are completely embedded by a flat layer of silicon dioxide that constricts a large amount of the sensing volume within the oxide layer itself. For corrugated sensors, the sensing volume is all around the protruding antennas but for the milled sensors the sensing volume is greatly decreased due to the oxide layer around the sides of the disks. Since the decay length, which determines the sensing volume, is an exponentially decaying parameter, it is weaker nearer the limits of its reach. Due to this, it is possible that the remaining sensing volume on top of the oxide above the small disks has a weaker interaction with the surrounding medium than otherwise seen from the same disk in a corrugated sensor. The longer decay length of the larger disks means that the effect of the extra oxide on the sensitivity is not as extreme.



*Figure 43. A plot of the BRIS sensitivity of the small antennas of flat sensors versus the remaining oxide thickness upon the sensor as measured with SEM. The best fit line suggests a decrease in BRIS as oxide thickness increases.*

The trend of the plot in Figure 43 suggests that the sensitivity of the smaller antennas is inversely proportional to the thickness of the oxide they are embedded in. This would support the hypothesis that it is oxide layer causing the decreased sensitivity.

## Adsorption Measurements

### Drift

One issue that affected the adsorption measurements was drift. This was prominent for all measurements ran on sensors embedded in silicon dioxide and significantly reduced or negligible for those embedded in silicon nitride. Although initial drift occurred after the addition of water to the measurement cell for both silicon dioxide and silicon nitride surfaces, baseline stabilization was achieved after approximately 1 hour. However, upon the introduction of a buffer solution, drift was sustained for those embedded in silicon dioxide. While this may not be a major concern for measurements lasting less than 10 minutes, for the systems measured in this project, where analyte binding to a lipid bilayer was on the scale of hours, this was an issue. To investigate the severity of the drift, two sensors, one embedded in silicon dioxide and one in silicon nitride, were soaked in various solutions over time and their spectra measured at different intervals. This result is shown below.

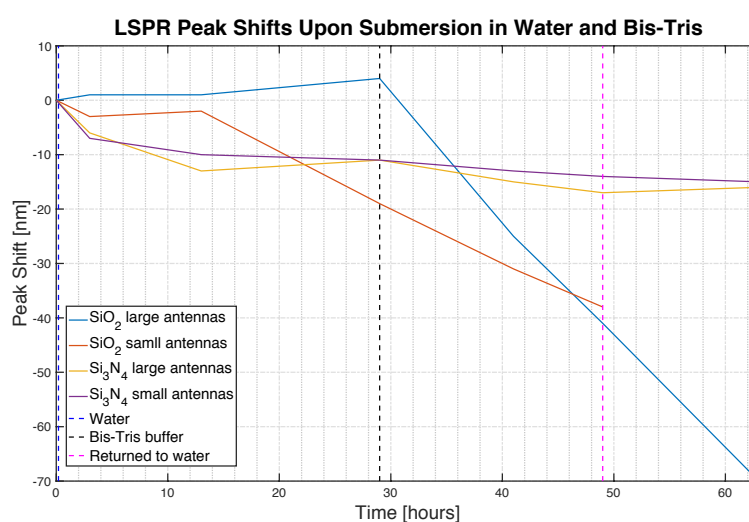


Figure 44. The LSPR shift for the large and small antennas of two sensors, one embedded in silicon dioxide and one in silicon nitride. The data was obtained by measuring the transmission spectra at various times over a 63 hour period and finding the wavelength corresponding to the minimum transmission. Measurements were taken after 3, 13, 29, 41, 49 and 63 hours. For the interval 0-29 hours the sensors were in MilliQ water, for 29-49 hours they were in bis-tris buffer and for 49-63 they were returned to water.

From Figure 44, it can clearly be seen that the drift for the SiO<sub>2</sub> embedded sensors in buffer solution is quite extreme. While submerged in water, the LSPR wavelength remains stable for the large antennas but upon submersion in buffer it decreases at a substantial rate. Interestingly, after the chip was returned to water, this decrease continues, which could imply that irreversible damage had occurred to the sensor's silver disks. Also, after completion of the submersion test, the small peak had completely vanished, which supports this. However, there is a substantial decrease in the LSPR wavelength for the small antennas after 29 hours in just water. This implies that the integrity of the SiO<sub>2</sub> layer may already have been compromised. After an initial decrease in the LSPR wavelengths for both antennas of the sensor embedded in Si<sub>3</sub>N<sub>4</sub>, they remained relatively stable throughout the submersion in buffer and return to water. It is known that Si<sub>3</sub>N<sub>4</sub> is more impenetrable to ions and water than PECVD produced SiO<sub>2</sub>. Since the decrease in the LSPR wavelength for the large antennas embedded in SiO<sub>2</sub> occurs at the

introduction of buffer and not at the introduction of water, it seems to suggest that the  $\text{SiO}_2$  layer may be affected by the ions contained in the buffer, most likely the sodium ions. It has been found that the presence of sodium ions in water can increase the rate of amorphous silica dissolution in water [46]. Therefore, if water had penetrated the  $\text{SiO}_2$ , as suggested by the shift for the small antennas at 29 hours, and sodium ions penetrated and promoted  $\text{SiO}_2$  dissolution, this could explain why the decrease in the LSPR wavelength for the  $\text{SiO}_2$  embedded chip was maintained after the chip was returned to water. The sodium ions may have catalysed sufficient dissolution of the silica surface to exposed the silver disks which then began to oxidise. Further investigation is necessary to determine the mechanism of the cause of the LSPR shift. However, this is out of the scope of this project. The result of interest for this project was the confirmation of a substantial and sustained drift of the LSPR wavelength for chips embedded in  $\text{SiO}_2$ . It is clear that  $\text{Si}_3\text{N}_4$  is a superior embedding material for these sensors.

### PLA adsorption

The first measurement that was attempted was a POPC and PLA adsorption measurement.

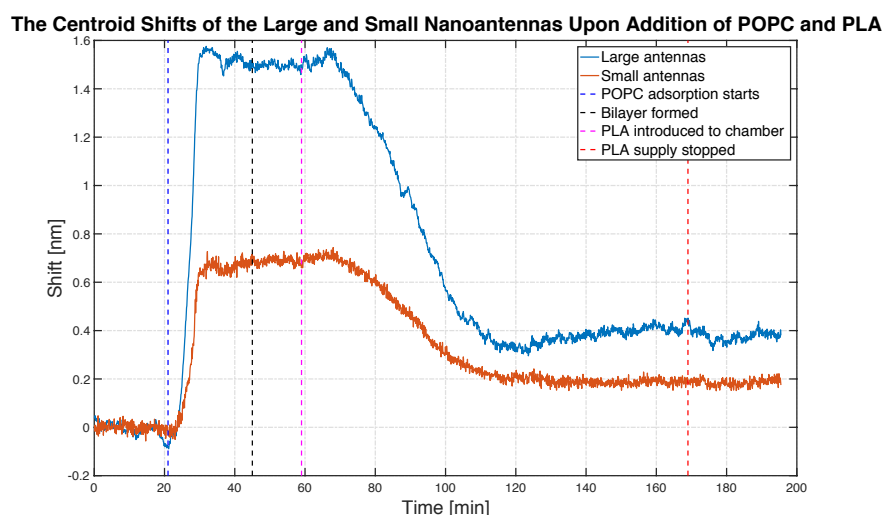


*Figure 45. A plot of the measured LSPR wavelength shifts for the centroids of the large and small antennas. Also highlighted on the plot are the times of POPC adsorption commencement, POPC bilayer formation, PLA introduction to the measurement cell and cessation of PLA addition followed by blank buffer reintroduction.*

Figure 45 shows the data obtained for the large and small antennas of an 80/210 nm milled sensor. The centroid was used for the data analysis in this case. This was due to the fact that it was less noisy. However, this data is also more noisy than ideal. The error due to this noise is 0.03 nm for the large antennas and 0.02 nm for the small antennas. This relatively large noise is due to the fact that the chip that was used for this measurement was a milled sensor which, as previously discussed, produced less sensitive sensors due to excessive oxide around the antennas. This data has also been corrected to remove drift, which occurred due to silicon dioxide being used as the embedding material. Correction was done by obtaining the slope of the baseline prior to POPC addition and subtracting this across the entire plot. Due to the relatively short measurement time the drift remained somewhat linear and correction was attainable.

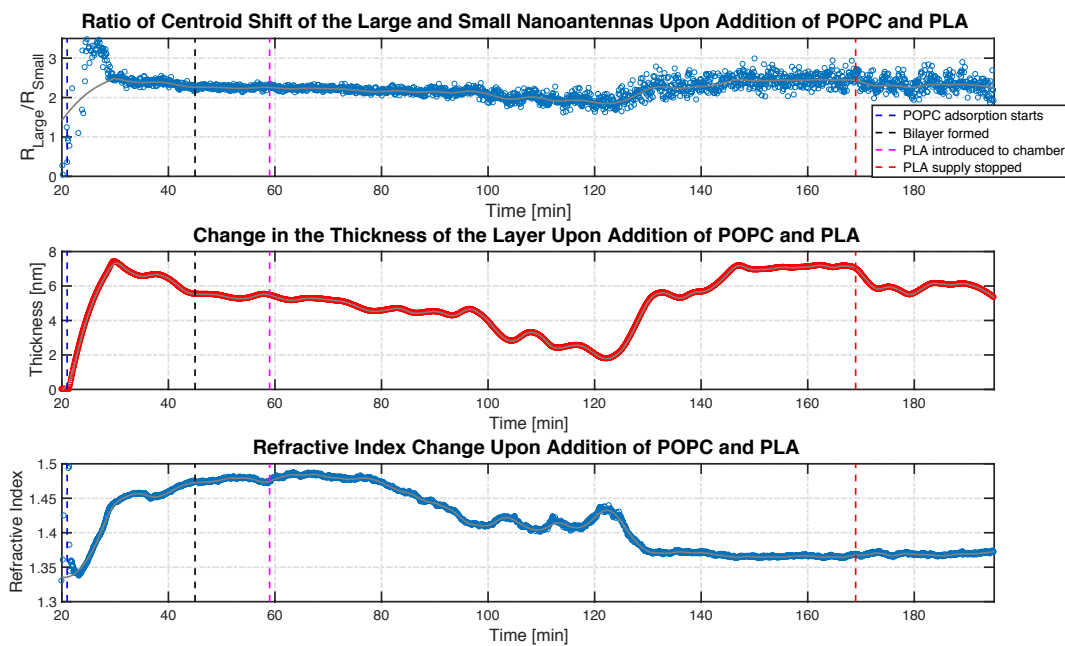


Figure 46. The calculated results from the data obtained for a POPC and PLA adsorption measurement carried out with a milled, flat sensor with a silicon dioxide surface. The figure shows the change in the ratio of the large and small centroids from Figure 45 over time, the change in the thickness of the layer on the surface of the sensor calculated from the local regression of this ratio (grey line) and variations in the refractive index of the layer over time. Also highlighted on the plots are the times of POPC adsorption commencement, POPC bilayer formation, PLA introduction to the measurement cell and cessation of PLA addition followed by blank buffer reintroduction.

The initial minutes of the introduction of POPC to the measurement chamber produces disordered and chaotic data, this is due to mixing within the chamber which can produce small changes in both the small and large antennas' spectra which results in large changes in their ratios. After POPC adsorption and stabilization of the baseline, the thickness of the layer on the surface of the sensor was determined to be  $\sim 5.5$  nm. The known thickness of a POPC bilayer is  $\sim 5$  nm and this value was used to determine the decay lengths for the sensor (equation 2.32), as previously shown. The reason for the difference of  $\sim 0.5$  nm between the two values is that equation 2.32 uses the shift of each peak separately in order to calculate the decay lengths for the antennas but the thickness plot uses the ratio of the two peaks, which in this case are excessively noisy. This noise only increases as the measurement continues, as can be seen from the ratio plot in Figure 46. This is due to the increased effect of the noise on the results as the total shift for each antenna decreases.

Between  $\sim 80$  and  $\sim 130$  minutes it is quite difficult to determine if the results are reliable due to the noise combined with the relatively long time over which a shift occurs. One also must remember that this data was corrected, opening up the possibility to some data being lost in the process. There may be sporadic binding of PLA and decomposition of the lipid layer to some degree, causing the apparent decrease in the layer thickness and refractive index but further measurements on sensors of a higher sensitivity would be necessary to confirm or invalidate these results before a mechanism for them could be established.

However, if we concentrate on the three “plateaus of stabilization” (Figure 45: 0 - 20 min, 45 - 60 min and 140 - 160 min) where signal saturation occurs there are points of interest. Obviously, 0-20 minutes is the beginning baseline, but it is an essential foundation of this sensing technique. This measurement is a good example of a bad baseline, one which was a lot worse before correction. In Figure 46, this baseline has been removed due to the lack of information of interest. Between 45 and 60 minutes it can be seen that the POPC layer is stable with a thickness of 5.26 – 5.5 nm and a measured refractive index of 1.476 – 1.479. This confirms the calibration of the sensor using the POPC layer and equation 2.32, albeit with some room for improvement going forward. The final plateau, between approximately 140 and 160 minutes shows an increase in the thickness of the layer on the sensor and a decrease in the refractive index. This may be due to the binding of PLA. PLA has a thickness of 2 – 2.2 nm and is believed to penetrate the surface of POPC upon binding by 0.5 nm [47] which would result in a thickness increase of 1.5 – 1.7 nm. The measured thickness increase on top of the POPC layer appears to be ~ 1.6 nm, which corresponds remarkably well with these results. However, this is complicated by the fact PLA hydrolyses POPC. Even if this process occurs over the duration of the measurement, it has been shown that an increase of the overall thickness of the layer would also be expected, but with an increase of ~ 0.9 nm in this case [48]. The sensor did detect a decrease in the refractive index to 1.366, which would be possible if PLA binding, as one might expect, disrupts the form of the lipid bilayer and decreases its refractive index. It would also be expected if POPC hydrolysis occurs.

After the PLA supply was stopped and buffer was pumped through the cell, there appears to be a decrease in the layer thickness but no significant change in the refractive index. This may be due to loosely associated PLA molecules being removed from the surface with the blank buffer.

This measurement showed that the concept for the sensor could certainly detect changes in thickness and refractive index but also highlighted the issues of drift and sensitivity caused by silica as the embedding material and excess oxide on the milled sensors, respectively. Further measurements with a more robust sensor would be required to test the reliability and reproducibility of the quantitative results. It was due to these issues that the remainder of the project focused on using silicon nitride embedded corrugated sensors for the adsorption measurements.

In saying that, when comparing the POPC adsorption for this milled sensor, Figure 45, and the same adsorption for a corrugated sensor, Figure 47, the decrease in the LSPR response is only a factor of 3. While this is certainly problematic for the signal to noise ratio, it is not extreme and is still manageable. When one considers the possible advantages of using a flat sensor, and the likelihood of increasing sensitivity by decreasing the oxide thickness, there is certainly an incentive for further research into these flat sensors in the future.

## DNA adsorption

POPC adsorption followed by DNA binding to the POPC bilayer was measured on a corrugated, silicon nitride embedded, sensor.

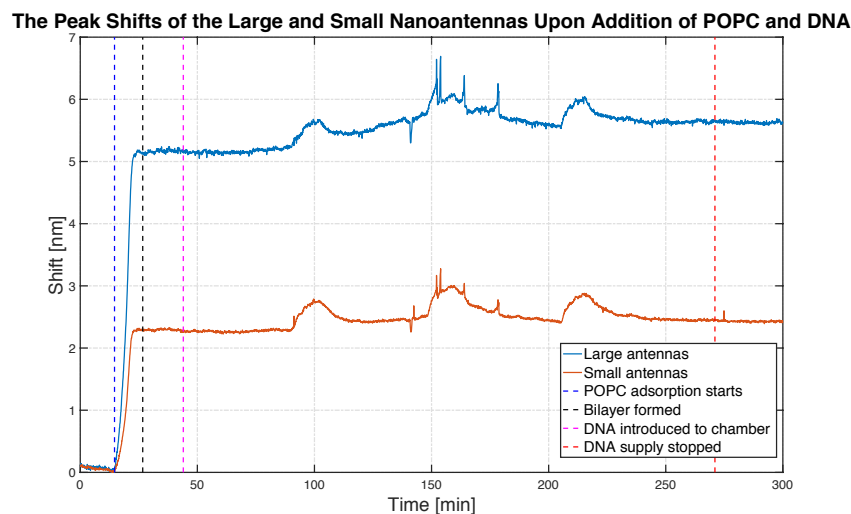


Figure 47. A plot of the measured LSPR wavelength shifts for the peaks of the large and small antennas. Also highlighted on the plot are the times of POPC adsorption commencement, POPC bilayer formation, DNA introduction to the measurement cell and cessation of DNA addition followed by blank buffer reintroduction.

For this measurement the peak shift gave the least noisy data and were therefore used for the data analysis. As can be seen from Figure 47, prior to POPC adsorption, there was some drift. However, upon the adsorption of POPC there was no longer any visible drift. It is quite possible that ions in the buffer were adsorbing to the surface of the sensor, causing the slight shift in the LSPR wavelength but the adsorption of POPC blocked these ions from the surface.

The error due to noise is 0.02 nm for both antennas. This is actually the same noise for the small antennas when compared to the milled sample. However, as previously mentioned, the signal is over 3 times greater for the adsorption of POPC on this sensor than for that of the milled sensor, resulting in superior signal to noise ratio for the corrugated sensor.

This measurement also highlights another potential issue with the measurement process. While it is possible that the anomalies seen between approximately 90 and 230 minutes are caused by conformational changes on the surface of the sensor, due to the rather capricious nature of the shifts it is more likely caused by air bubbles from the sample passing through the chamber. Thorough degassing of the sample would be required to mitigate this. However, similar to the PLA adsorption measurement there are three plateaus of stabilization for data analysis.

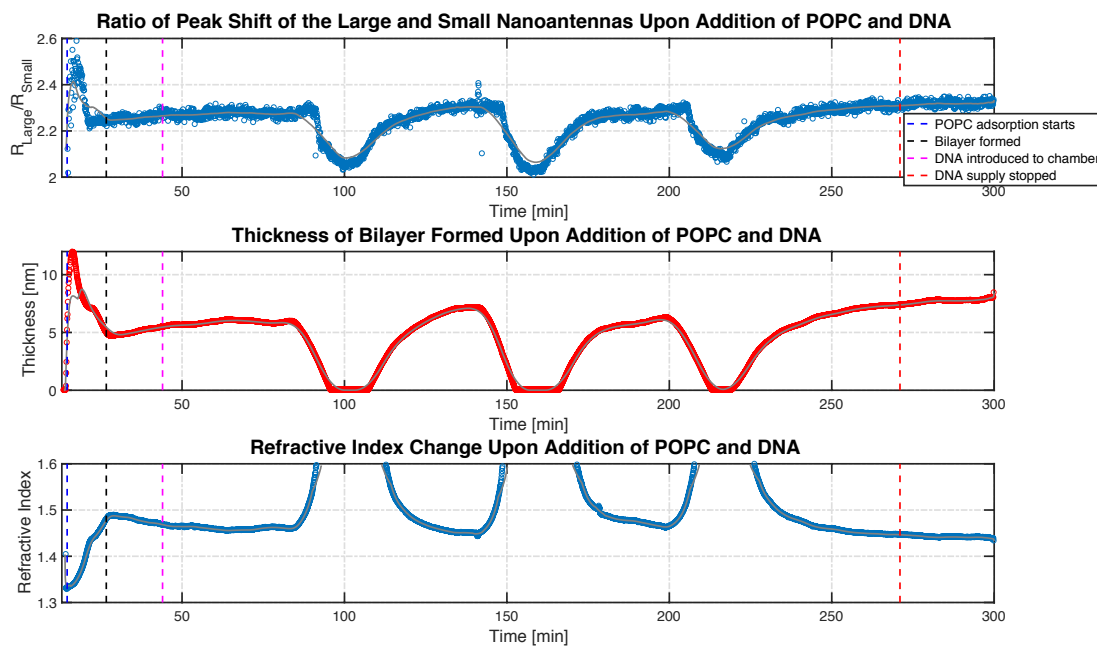


Figure 48. The calculated results from the data obtained for a POPC and DNA adsorption measurement carried out with a corrugated sensor with a silicon nitride surface. The figure shows the change in the ratio of the large and small peaks from Figure 47 over time, the change in the thickness of the layer on the surface of the sensor calculated from the local regression of this ratio (grey line) and variations in the refractive index of the layer over time. Also highlighted on the plots are the times of POPC adsorption commencement, POPC bilayer formation, DNA introduction to the measurement cell and cessation of DNA addition followed by blank buffer reintroduction.

The first thing that one notices is that the effect of the anomalies in the raw data becomes exacerbated in the calculated results. This is to be expected in a technique that has ratio-based calculations. This highlights the need for a pure, degassed sample. It can also be seen that the noise from the raw data is also exacerbated in the ratio plot. However, when compared to the ratio data for the PLA adsorption measurements on a milled sensor (Figure 46) there is an obvious decrease in this noise. This is due to the increase in the signal that is characteristic to a corrugated sensor over a milled one.

Due to these anomalies, it is very difficult to hypothesise on the meaning of the data between approximately 80 and 240 minutes since it is unknown what data may be lost within these apparently erratic changes. Again, similar to the PLA adsorption data analysis we can focus on the three plateaus of stabilization. The baseline prior to POPC adsorption was somewhat stable. There was some drift which, as can be seen from the submersion test, will still occur for silicon nitride surfaces but this drift is less severe than silicon dioxide surfaces and did not continue beyond POPC adsorption which negated the need for correction. The second plateau, between 25 and 45 minutes, corresponds to the time between bilayer formation and DNA introduction and was again used for confirmation of sensor calibration. The measured thickness was found to be  $\sim 5 - 5.4$  nm and the refractive index  $1.47 - 1.488$  over this range. The deviation from the expected values is again most likely due to the noise found in the raw data. The final plateau after  $\sim 280$  minutes shows a final thickness of  $7.74$  nm and a refractive index of  $1.441 - 1.442$ . The length of ABCD – DNA was known to be approximately  $15$  nm. However, it is quite possible that the DNA lay upon the lipid in a sideways confirmation and

not lengthways upon binding. The diameter of DNA is approximately 2 nm, similar to the value detected here. Similar to the PLA adsorption measurement, the decrease in the refractive index is most likely due to disruption of the lipid bilayer by DNA binding. ABCD-DNA binding is less extensive than PLA binding and this could explain the why the refractive index shift is less for the DNA.

Again, this measurement displayed the sensor's ability to detect changes in the thickness and refractive index of a layer while highlighting areas for optimization, the primary area in this case being the degassing of all samples prior to the measurement process.

## 7. Conclusion

Two types of dual-sized nanoantennas sensors were successfully fabricated, corrugated and flat. For both of these types, it has been shown that LSPR wavelengths of the peaks used for analysis could be tuned using various PS bead sizes in the HCL fabrication process. The only limit placed on this being a minimum diameter difference of approximately 100 nm to ensure good peak separation for individual peak tracking. Spectral blue-shifting was experienced upon the deposition of the embedding layer via PECVD, with silicon dioxide deposition causing the largest shift, which must be considered if specific LSPR wavelength ranges for the antennas are desired.

The milling of corrugated chips with thick oxide layers using specific parameters has been applied to produce a large decrease in roughness leading to the fabrication of topographically flat sensors. On average, the roughness achieved using these parameters was consistently found to be  $\sim 10$  times lower than that of a corrugated sensor of the same disk diameters. The sensitivity of these sensors is somewhat decreased by the presence of extra dielectric enveloping the antennas. However, adsorption measurements with these sensors were successfully carried out and it has also been shown that the adsorption of lipids to these sensors was significantly faster than on the corrugated sensors. In saying that, it was also shown that stable lipid bilayers could be formed and maintained on the corrugated sensors with no apparent decrease in stability due to this corrugation. Along these lines, there is also no apparent difference in the stability of an adsorbed bilayer on a silicon nitride surface versus a silicon dioxide surface.

For the adsorption measurements, it was found that drift was a prominent issue. Submersion tests concluded that this issue was emphatically more extreme for a silicon dioxide surface than a silicon nitride surface when in the presence of a buffer solution.

Successful adsorption measurements were carried out using POPC followed by the binding of a protein or a DNA to this lipid bilayer. This included the development of a measurement technique, wherein the calibration of the sensor and the adsorption of the DNA or protein were both facilitated by the POPC lipid bilayer. Both measurements successfully detected changes in the layer thickness and refractive indices. Qualitatively, the results of the measurements on both systems produced results that were in line with those found in literature.

### *Outlook*

The technique used for the fabrication of these sensors is quite flexible in terms of disk size and material composition. Due to some oxidation issues with silver, it may be interesting to investigate the use of other plasmonic materials for the fabrication of the dual-sized antennas, including gold. Although the interband transition for gold lies around 470 nm [49], which reduces the range over which peak separation can be achieved to  $\sim 500$  nm, as opposed to  $\sim 600$  nm for silver, it has been shown in this project that successful peak tracking can be obtained with a peak separation of less than 250 nm. This opens up the possibility to fabricate sensors using gold which is more robust than silver and would not require embedding for a corrugated sensor.

Due to the substantial drift experienced with silicon dioxide it would be prudent to focus future optimization fabrications and measurements on sensors embedded in silicon nitride. This includes for the milling process, which had been optimized primarily towards the removal of

silicon dioxide. The targeted thickness of the final nitride layer should also be reduced to  $< 5$  nm above the antennas to improve the sensitivity for these milled sensors.

Further adsorption measurements with nitride embedded sensors should be carried out. While the investigation into other systems would be quite interesting and may be tempting it would be advisable to perform multiple measurements on the same systems, perhaps those used in this project, to evaluate the reliability and reproducibility of the results obtained here. In saying that, the subtleties involved for the PLA binding process may be too complex to use as a “proof of principle” system. Regardless of what system is used, these measurements should also be executed in parallel with a technique such as that found in [20] to assess the quantitative data obtained using the sensor.

Although there remains some optimization to the fabrication and measurement procedures described in this report, a functional dual-sized nanoantennas sensor has been produced, including in a topographically flat form. It has also been shown that this sensor facilitates the simultaneous determination of changes in the thickness and refractive index of a layer upon its surface. In this project that layer was a lipid bilayer but the process is not confined to this. The use of a lipid bilayer highlights the potential of this sensor in biological studies. Since a large focal point of this field is on the interactions of molecules with cell membranes this sensor is ideal for the investigation of binding and conformational changes on, or within, these lipid bilayers.

## 8. Bibliography

- [1] “National Nanotechnology Initiative,” [Online]. Available: <https://www.nano.gov/nanotech-101/what/nano-size>. [Accessed 16 May 2017].
- [2] R. Feynman, “Caltech,” February 1960. [Online]. Available: <http://calteches.library.caltech.edu/47/2/1960Bottom.pdf>. [Accessed 31 January 2017].
- [3] A. Pratt, L. Lari, O. Hovorka, A. Shah, C. Woffinden, S. P. Tear, C. Binns and R. Kröger, “Enhanced oxidation of nanoparticles through strain-mediated ionic transport,” *Nat Mater*, vol. 13, no. 1, pp. 26-30, 2014.
- [4] O. Petravic, “Superparamagnetic nanoparticle ensembles,” *Superlattices and Microstructures*, vol. 47, no. 5, pp. 569-578, 2010.
- [5] A. V. Whitney, J. W. Elam, S. Zou, A. V. Zinovev, P. C. Stair, G. C. Schatz and R. P. Van Duyne, “Localized Surface Plasmon Resonance Nanosensor: A High-Resolution Distance-Dependence Study Using Atomic Layer Deposition,” *The Journal of Physical Chemistry B*, vol. 109, no. 43, pp. 20522-20528, 2005.
- [6] J. J. Mock, D. R. Smith and S. Schultz, “Local Refractive Index Dependence of Plasmon Resonance Spectra from Individual Nanoparticles,” *Nano Letters*, vol. 3, no. 4, pp. 485-491, 2003.
- [7] E. M. Larsson, C. Langhammer, I. Zorić and B. Kasemo, “Nanoplasmonic Probes of Catalytic Reactions,” *Science*, vol. 326, no. 5956, pp. 1091--1094, 2009.
- [8] G. Mie, “Beiträge zur Optik trüber Medien, speziell kolloidaler Metallösungen,” *Ann. Phys.*, vol. 330, no. 3, pp. 377-445, 1908.
- [9] Eusebius, “Chartres Cathedral,” 7 February 2009. [Online]. Available: [https://en.wikipedia.org/wiki/Chartres\\_Cathedral#/media/File:Chartres\\_-\\_cathédrale\\_-\\_rosace\\_nord.jpg](https://en.wikipedia.org/wiki/Chartres_Cathedral#/media/File:Chartres_-_cathédrale_-_rosace_nord.jpg). [Accessed 1 February 2017].
- [10] MOSSOT, “Chartres Cathedral,” 10 August 2010. [Online]. Available: [https://en.wikipedia.org/wiki/Stained\\_glass#/media/File:Chartres\\_-\\_Vitrail\\_de\\_la\\_Vie\\_de\\_Joseph.JPG](https://en.wikipedia.org/wiki/Stained_glass#/media/File:Chartres_-_Vitrail_de_la_Vie_de_Joseph.JPG). [Accessed 1 February 2017].
- [11] M. I. Stockman, “Nanoplasmonics: The physics behind the applications,” *Physics Today*, vol. 64, no. 2, pp. 39-44, 2011.
- [12] T. Yuhi, N. Nagatani, T. Endo, K. Kerman, M. Takata, H. Konaka, M. Namiki, Y. Takamura and E. Tamiya, “Gold nanoparticle based immunochromatography using a resin modified micropipette tip for rapid and simple detection of human chorionic gonadotropin hormone and prostate-specific antigen,” *Science and Technology of Advanced Materials*, vol. 7, no. 3, p. 276, 2006.
- [13] R. Wang, S. Zuo, D. Wu, J. Zhang, W. Zhu, K. H. Becker and J. Fang, “Microplasma-Assisted Synthesis of Colloidal Gold Nanoparticles and Their Use in the Detection of Cardiac Troponin I (cTn-I),” *Plasma Processes and Polymers*, vol. 12, no. 4, pp. 380-391, 2015.
- [14] D. S. Kim, Y. T. Kim, S. B. Hong, J. Kim, N. S. Heo, M.-K. Lee, S. J. Lee, B. I. Kim, I. S. Kim, Y. S. Huh and B. G. Choi, “Development of Lateral Flow Assay Based on Size-Controlled Gold Nanoparticles for Detection of Hepatitis B Surface Antigen,” *Sensors*, vol. 16, no. 12, 2016.
- [15] Y. N. Tan, X. Su, Y. Zhu and J. Y. Lee, “Sensing of Transcription Factor through Controlled-Assembly of Metal Nanoparticles Modified with Segmented DNA Elements,” *ACS Nano*, vol. 4, no. 9, pp. 5101-5110, 2010.

- [16] J. A. Maynard, N. C. Lindquist, J. N. Sutherland, A. Lesuffleur, A. E. Warrington, M. Rodriguez and S.-H. Oh, "Next generation SPR technology of membrane-bound proteins for ligand screening and biomarker discovery," *Biotechnol J*, vol. 4, no. 11, pp. 1542-1558, 2009.
- [17] A. Das, J. Zhao, G. C. Schatz, S. G. Sligar and R. P. Van Duyne, "Screening of Type I and II Drug Binding to Human Cytochrome P450-3A4 in Nanodiscs by Localized Surface Plasmon Resonance Spectroscopy," *Analytical Chemistry*, vol. 81, no. 10, pp. 3754-3759, 2009.
- [18] S.-W. Lee, K.-S. Lee, J. Ahn, J.-J. Lee, M.-G. Kim and Y.-B. Sing, "Highly Sensitive Biosensing Using Arrays of Plasmonic Au Nanodisks Realized by Nanoimprint Lithography," *ACS Nano*, vol. 5, no. 2, pp. 897-904, 2011.
- [19] P. Tabib Zadeh Adibi, F. Mazzotta, T. J. Antosiewicz, M. Skoglundh, H. Grönbeck and C. Langhammer, "In Situ Plasmonic Sensing of Platinum Model Catalyst Sintering on Different Oxide Supports and in O<sub>2</sub> and NO<sub>2</sub> Atmospheres with Different Concentrations," *ACS Catalysis*, vol. 5, no. 1, pp. 426-432, 2015.
- [20] M. P. Jonsson, P. Jönsson and F. Höök, "Simultaneous Nanoplasmonic and Quartz Crystal Microbalance Sensing: Analysis of Biomolecular Conformational Changes and Quantification of the Bound Molecular Mass," *Analytical Chemistry*, vol. 80, no. 21, pp. 7988-7995, 2008.
- [21] Y.-C. Chang, H.-C. Chung, S.-C. Lu and T.-F. Guo, "A large-scale sub-100 nm Au nanodisk array fabricated using nanospherical-lens lithography: a low-cost localized surface plasmon resonance sensor," *Nanotechnology*, vol. 24, no. 9, p. 095302, 2013.
- [22] F. A. A. Nugroho, R. Frost, T. J. Antosiewicz, J. Fritzsche, E. M. Larsson Langhammer and C. Langhammer, "Topographically Flat Nanoplasmonic Sensor Chips for Biosensing and Materials Science," *ACS Sensors*, 9 December 2016.
- [23] A. Alabastri, S. Tuccio, A. Giugni, A. Toma, C. Liberale, G. Das, F. D. Angelis, E. D. Fabrizio and R. P. Zaccaria, "Molding of Plasmonic Resonances in Metallic Nanostructures: Dependence of the Non-Linear Electric Permittivity on System Size and Temperature.," *Materials*, vol. 6, no. 11, pp. 4879-4910, 2013.
- [24] A. Moroz, "Wave-scattering.com," [Online]. Available: <http://www.wave-scattering.com/drudefit.html>. [Accessed 07 04 2017].
- [25] W. L. Barnes, "Particle plasmons: Why shape matters," *Am. J. Phys.*, vol. 84, no. 593, 2016.
- [26] L. S. Jung, C. T. Campbell, T. M. Chinowsky, M. N. Mar and S. S. Yee, "Quantitative Interpretation of the Response of Surface Plasmon Resonance Sensors to Adsorbed Films," *Langmuir*, vol. 14, no. 19, pp. 5636-5648, 1998.
- [27] D. L. M. Rupert, G. V. Shelke, G. Emilsson, V. Claudio, S. Block, C. Lässer, A. Dahlin, J. O. Lötvall, M. Bally, V. P. Zhdanov and F. Höök, "Dual-Wavelength Surface Plasmon Resonance for Determining the Size and Concentration of Sub-Populations of Extracellular Vesicles," *Analytical Chemistry*, vol. 88, no. 20, pp. 9980-9988, 2016.
- [28] H. Fredriksson, Y. Alaverdyan, A. Dmitriev, C. Langhammer, D. S. Sutherland, M. Zäch and B. Kasemo, "Hole-Mask Colloidal Lithography," *Advanced Materials*, no. 19, pp. 4297-4302, 2007.
- [29] MicroChem, "MicroChem Corp.," 2001. [Online]. Available: [http://microchem.com/pdf/PMMA\\_Data\\_Sheet.pdf](http://microchem.com/pdf/PMMA_Data_Sheet.pdf). [Accessed 4 May 2017].
- [30] V. Jokinen, P. Suvanto and S. Franssila, "Oxygen and nitrogen plasma hydrophilization and hydrophobic recovery of polymers," *Biomicrofluidics*, vol. 6, no. 1, pp. 016501-10, 3 January 2012.
- [31] M. Moravej, S. E. Babayan, G. R. Nowling, X. Yang and R. F. Hicks, "Plasma enhanced chemical vapour deposition of hydrogenated amorphous silicon at atmospheric pressure," *Plasma Sources Science and Technology*, vol. 13, no. 1, p. 8, 2004.

- [32] D. H. Jang, J. S. Chun and J. G. Kim, "The deposition rate and properties of the deposit in plasma enhanced chemical vapor deposition of TiN," *Journal of Vacuum Science & Technology A: Vacuum, Surfaces, and Films*, vol. 7, no. 1, pp. 31-35, 1989.
- [33] S. Mornet, O. Lambert, E. Duguet and A. Brisson, "The Formation of Supported Lipid Bilayers on Silica Nanoparticles Revealed by Cryoelectron Microscopy," *Nano Letters*, vol. 5, no. 2, pp. 281-285, 2005.
- [34] P. Nollert, H. Kiefer and F. Jähnig, "Lipid vesicle adsorption versus formation of planar bilayers on solid surfaces," *Biophysical Journal*, vol. 69, no. 4, pp. 1447 - 1455, 1995.
- [35] M. Lundqvist, I. Sethson and B.-H. Jonsson, "Protein Adsorption onto Silica Nanoparticles: Conformational Changes Depend on the Particles' Curvature and the Protein Stability," *Langmuir*, vol. 20, no. 24, pp. 10639-10647, 2004.
- [36] M. Hagberg, Artist, *Kuafman Ion Source*. [Art]. Chalmers Institute of Technology, Cleanroom.
- [37] A. Varbel, Dimension (TM) 3100 Manual, Digital Instruments Veeco Metrology Group.
- [38] C. Kowalski, NanoScope Software 6.12 User Guide, Veeco Instruments Inc..
- [39] P. Jedrasik, "myfabLIMS," [Online]. Available: <http://labbokning.mc2.chalmers.se/WebForms/Equipment/EquipmentView.aspx?toolId=187>. [Accessed 11 May 2017].
- [40] "Insplorion XNano II Product Information," Insplorion, [Online]. Available: <https://www.insplorion.com/app/uploads/InsplorionXNanoIIWeb.pdf>. [Accessed 15 May 2017].
- [41] A. B. Dahlin, J. O. Tegenfeldt and F. Höök, "Improving the Instrumental Resolution of Sensors Based on Localized Surface Plasmon Resonance," *Analytical Chemistry*, vol. 78, no. 13, pp. 4416-4423, 2006.
- [42] Physical properties of glycerine and its solutions., New York: Glycerine Producers' Association, 1963.
- [43] P. C. Dave, E. K. Tiburu, K. Damodaran and G. A. Lorigan, "Investigating Structural Changes in the Lipid Bilayer upon Insertion of the Transmembrane Domain of the Membrane-Bound Protein Phospholamban Utilizing <sup>31</sup>P and <sup>2</sup>H Solid-State NMR Spectroscopy," *Biophysical Journal*, vol. 86, no. 3, pp. 1564-1573, 2004.
- [44] A. Mashaghi, M. Swann, J. Popplewell, M. Textor and E. Reimhult, "Optical Anisotropy of Supported Lipid Structures Probed by Waveguide Spectroscopy and Its Application to Study of Supported Lipid Bilayer Formation Kinetics," *Analytical Chemistry*, vol. 80, no. 10, pp. 3666-3676, 2008.
- [45] W. Lau, P. Qian, T. Han, N. P. Sandler, S. Che, S. Ang, C. Tung and T. Sheng, "Evidence that N<sub>2</sub>O is a stronger oxidizing agent than O<sub>2</sub> for both Ta<sub>2</sub>O<sub>5</sub> and bare Si below 1000 °C and temperature for minimum low-K interfacial oxide for high-K dielectric on Si," *Microelectronics Reliability*, vol. 47, no. 2-3, pp. 429-433, 2007.
- [46] J. P. Icenhower and P. M. Dove, "The dissolution kinetics of amorphous silica into sodium chloride solutions: effects of temperature and ionic strength," *Geochimica et Cosmochimica Acta*, vol. 64, no. 24, pp. 4193-4203, 2000.
- [47] H. P. Vacklin, F. Tiberg, G. Fragneto and R. K. Thomas, "Phospholipase A<sub>2</sub> Hydrolysis of Supported Phospholipid Bilayers: A Neutron Reflectivity and Ellipsometry Study," *Biochemistry*, vol. 44, no. 8, pp. 2811-2821, 2005.

- [48] H. P. Wacklin, F. Tiberg, G. Fragneto and R. K. Thomas, "Distribution of reaction products in phospholipase A2 hydrolysis," *Biochimica et Biophysica Acta (BBA) - Biomembranes*, vol. 1768, no. 5, pp. 1036-1049, 2007.
- [49] P. G. Etchegoin, E. C. Le Ru and M. Meyer, "An analytic model for the optical properties of gold," *The Journal of Chemical Physics*, vol. 125, no. 16, p. 164705, 2006.